

Title	Large-Eddy-Simulation Study of the Effects of Building-Height Variability on Turbulent Flows over an Actual Urban Area
Author(s)	Yoshida, Toshiya; Takemi, Tetsuya; Horiguchi, Mitsuaki
Citation	Boundary-Layer Meteorology (2018), 168(1): 127-153
Issue Date	2018-07
URL	<a href="http://hdl.handle.net/2433/231409">http://hdl.handle.net/2433/231409</a>
Right	The final publication is available at Springer via <a href="https://doi.org/10.1007/s10546-018-0344-8">https://doi.org/10.1007/s10546-018-0344-8</a> ; The full-text file will be made open to the public on 03 March 2019 in accordance with publisher's 'Terms and Conditions for Self-Archiving'.; This is not the published version. Please cite only the published version. この論文は出版社版ではありません。引用の際には出版社版をご確認ご利用ください。
Type	Journal Article
Textversion	author

1 **Large-Eddy-Simulation Study on the Effects of**  
2 **Building-Height Variability on Turbulent Flows over**  
3 **an Actual Urban Area**

4 **Toshiya Yoshida · Tetsuya Takemi ·**  
5 **Mitsuaki Horiguchi**

6 Received: DD Month YEAR / Accepted: DD Month YEAR

7 **Abstract** A large-eddy simulation (LES) was conducted to investigate the ef-  
8 fects of building-height variability on turbulent flows over an actual urban area,  
9 the city of Kyoto, which was reproduced using a 2-m resolution digital surface  
10 dataset. Comparison of the morphological characteristics of Kyoto with those of  
11 European, North American, and other Japanese cities indicates a similarity to  
12 European cities but with more variable building heights. The performance of the  
13 LES model is validated and found to be consistent with turbulence observations  
14 obtained from a meteorological tower and Doppler lidar. We conducted the follow-  
15 ing two numerical experiments: a control experiment using Kyoto buildings, and  
16 a sensitivity experiment in which all the building heights are set to the average  
17 height over the computational region  $h_{all}$ . The difference of Reynolds stress at

---

Toshiya yoshida · Tetsuya Takemi · Mitsuaki Horiguchi

Disaster Prevention Research Institute, Kyoto University, Kyoto, Japan

E-mail: yoshida.t@storm.dpri.kyoto-u.ac.jp

18 height  $z = 2.5h_{all}$  between the control and sensitivity experiments is found to  
19 increase with the increase in the plan-area index ( $\lambda_p$ ) for  $\lambda_p > 0.32$ . Thus, values  
20 of  $\lambda_p$  of around 0.3 can be regarded as a threshold for distinguishing the effects of  
21 building-height variability. The quadrant analysis reveals that sweeps contribute to  
22 the increase in the Reynolds stress in the control experiment at height  $z = 2.5h_{all}$ .  
23 The exuberance in the control experiment at height  $z = 0.5h_{all}$  is found to de-  
24 crease with an increase in the building-height variability. Although the extreme  
25 momentum flux at height  $z = 2.5h_{all}$  in the control experiment appears around  
26 buildings, it contributes little to the total Reynolds stress and is not associated  
27 with coherent motion.

28 **Keywords** Actual urban building · Large-eddy simulation · Atmospheric  
29 turbulence · Roughness parameter · Reynolds stress · Quadrant analysis

## 30 1 Introduction

31 Atmospheric processes over urban areas are affected not only by meteorological  
32 disturbances, such as thunderstorms, fronts, and cyclones, but also by the rough-  
33 ness and thermal effects of buildings and man-made structures. The geometrical  
34 features of buildings and structures determine the roughness effects of an urban  
35 area, while human activities and the material characteristics of buildings play a  
36 role in defining the thermal effects of such areas. The complex geometrical nature  
37 of urban surfaces results in highly complex turbulent flows. To properly under-  
38 stand the physical processes of momentum and heat transfer in urban areas and  
39 develop parametrizations for urban environments in numerical weather prediction

40 models, it is important to reveal relationships between the effects of actual urban  
41 buildings and turbulent flows.

42 The characteristics of turbulent flows over urban surfaces have been examined  
43 in numerous previous studies. Oke (1988) categorized the airflow over roughness  
44 obstacles as a function of obstacle density as isolated flows, wake-interference flows,  
45 and skimming flows. Macdonald et al. (1998) derived a theoretical relation for the  
46 aerodynamic roughness length  $z_0$  and displacement height  $d$  for flows over rough-  
47 ness blocks. While these studies examined turbulent flows over roughness blocks  
48 with constant height and regular distribution, the recent focus has shifted to the  
49 effects on turbulent flows of roughness blocks with variable height and inhom-  
50 geneous arrangement. Wind-tunnel experiments conducted by Cheng and Castro  
51 (2002) demonstrated that the roughness sublayers over block arrays with random  
52 height are thicker than those over uniform-height arrays. Xie et al. (2008) con-  
53 ducted a large-eddy simulation (LES) of turbulent flows over block arrays with  
54 random height, and found that the tall blocks significantly contribute to the total  
55 drag of such arrays. Nakayama et al. (2011) performed LES investigations over  
56 building arrays with different height variability and found that the vertical pro-  
57 files of the mean velocity and Reynolds stress depend significantly on the building-  
58 height variability. Zaki et al. (2011) performed wind-tunnel experiments with block  
59 arrays of buildings with variable height distributed randomly, and showed that the  
60 drag coefficient  $C_d$  increases with the building density and the standard deviation  
61 of the building height for high building densities. Numerical simulations of plume  
62 dispersion over urban surfaces have revealed that the turbulence is significantly  
63 affected by the source location and wind direction because of the strong depen-  
64 dence on the building height and distribution. (Xie and Castro 2009; Xie 2011;

65 Nakayama et al. 2016). The parametrizations of  $z_0$  and  $d$  have been improved by  
66 taking into account roughness parameters associated with actual urban buildings,  
67 such as the maximum, standard deviation, and skewness of the building height  
68 (Nakayama et al. 2011; Kanda et al. 2013; Zhu et al. 2017). Giometto et al. (2016)  
69 suggested that the dispersive flux derived from spatial variations of temporal mean  
70 flows around buildings should be considered to improve conventional urban-canopy  
71 parametrizations.

72 To fully understand the effects of roughness obstacles on turbulent flows, it  
73 is helpful to investigate the relationships between turbulent organized structures  
74 and obstacles, because organized structures are associated with downwards mo-  
75 mentum transfer in the form of ejection and sweep events based on a quadrant  
76 analysis for the turbulent momentum flux. The results of wind-tunnel experiments  
77 on flows over rough surfaces conducted by Raupach (1981) indicate that sweeps  
78 are dominant for the total momentum flux near surfaces, and that the contribu-  
79 tion of ejection to the momentum flux increases with height. Studies in which  
80 turbulence was observed over actual urban areas have revealed the characteristics  
81 of momentum transfer and coherent motion. Oikawa and Meng (1995) observed  
82 turbulent structures associated with ejections and sweeps over an urban area, and  
83 found that turbulent structures correlate with heat transfer within and above the  
84 urban canopy. Christen et al. (2007) analyzed field experimental data obtained  
85 from sonic-anemometer measurements within and above a street canyon in Basel,  
86 Switzerland, and found that sweeps are mostly dominant up to a height of approxi-  
87 mately twice the average building height in a street canyon. Numerical simulations  
88 of flows over building arrays have revealed the spatial characteristics of turbulent  
89 organized structures. Kanda et al. (2004) carried out LES investigations of tur-

90 bulent flows over uniform-height block arrays to investigate turbulent organized  
91 structures over such arrays. They found low-speed streaks and streamwise vortices  
92 similar to those in flows over flat-wall boundary layers. Kanda (2006) indicated  
93 that streak structures are a common feature over various types of block arrays.  
94 Using direct numerical simulations, Coceal et al. (2007a,b) revealed that hairpin  
95 vortices associated with ejections and sweeps are generated over uniform block  
96 arrays, and that the low-speed streaks identified above such arrays are composed  
97 of large numbers of hairpin vortices aligned in the streamwise direction. Park et al.  
98 (2015) used LES results to analyze turbulent-flow structures over an actual urban  
99 area in Seoul, Korea, and showed that turbulent structures behind high-rise build-  
100 ings are characterized by streamwise vortices with strong ejections. They focused  
101 on small regions containing high-rise buildings, and demonstrated the significant  
102 influence of high-rise buildings on wake flows. The majority of studies presented  
103 thus far have focused on the characteristics of turbulent flows over idealized or  
104 specific buildings, while only a few have examined the urban-scale effects on the  
105 characteristics of turbulent momentum transfer produced by the complex geomet-  
106 rical features of actual urban surfaces.

107 The geometrical characteristics of actual urban surfaces can be reproduced  
108 from digital surface datasets. Ratti et al. (2002) calculated the roughness param-  
109 eters of North American and European cities, and found that parameters differ  
110 significantly by city. Bou-Zeid et al. (2009) indicated that turbulent flows are  
111 dependent on the building representation over the actual urban surface. To un-  
112 derstand the characteristics of turbulent flows over urban areas, it is therefore  
113 important to use the geometry of actual buildings in simulations and experiments.

114 We investigate here the effects of building-height variability in an actual urban  
115 area on turbulent flows at an urban scale, focusing on the airflow within and above  
116 an urban-canopy layer, where turbulent flows are strongly influenced by individual  
117 buildings.

118 We simulate the turbulent flow over the urban area of Kyoto, which is charac-  
119 terized by the presence of both business districts with high buildings and densely  
120 built residential districts. Furthermore, a meteorological observation tower owned  
121 by Kyoto University and located in the southern part of the city can be used for  
122 the validation of simulations. In Sect. 2, the building morphological characteris-  
123 tics of Kyoto are evaluated using roughness parameters. The details of our LES  
124 model are described in Sect. 3. The study area of the LES investigation is defined  
125 to include the meteorological tower site at which turbulence was measured by a  
126 sonic anemometer and Doppler lidar, so that LES results may be compared with  
127 the observations (see Sect. 4). Along with a control simulation, we conduct a sen-  
128 sitivity test assuming a constant building height to reveal the effects of building  
129 height–height variability, with the differences between the control and sensitivity  
130 experiments examined in Sect. 5. Finally, Sect. 6 concludes the paper.

## 131 **2 Building Morphological Characteristics of Kyoto**

132 Our study area covered both business districts and suburban areas in Kyoto. Fig-  
133 ure 1 shows the area of interest in Kyoto, which extends 11 km in a north–south  
134 direction and by 2 km in an east–west direction. A digital surface model (Koku-  
135 sai Kogyo Co., Ltd.) was used to reproduce the actual urban buildings within a  
136 numerical model. The original 2-m-resolution data are smoothed and converted

137 to a 4-m resolution, which is used as the horizontal grid spacing of the numerical  
138 experiments as described in Sect. 3.2.

139 Figure 2a shows the height of the actual buildings in the analysis area. The  
140 north–south and west–east directions are referred to as the  $x$  and  $y$  directions,  
141 respectively. The region with  $x = 0 - 4$  km corresponds to the city centre of  
142 Kyoto. The heights of almost all buildings in the region are up to 50 m, and there  
143 are no high-rise building clusters of the type seen in the centre of Tokyo. The  
144 region for  $x = 7 - 11$  km is primarily occupied by suburban areas and rivers.

145 The difference between the building heights over these two regions is clearly  
146 indicated in Fig. 2b, which shows the frequency distributions of building heights  
147 over the entire analysis area and in the  $x = 0 - 4$  km and  $x = 7 - 11$  km regions. In  
148 calculating the frequency distributions, all buildings are defined as having heights  
149 of at least 1 m to distinguish between the buildings and the ground. It is seen that  
150 most of the buildings taller than 25 m are located in the former region.

151 To quantitatively indicate the morphological characteristics of buildings in Ky-  
152 oto, we use roughness parameters such as the average building height  $H_{ave}$ , the  
153 standard deviation of the building height  $\sigma_H$ , the plan-area index  $\lambda_p$  (the ratio of  
154 the plan area occupied by buildings to the total surface area), and the frontal-area  
155 index  $\lambda_f$  (the ratio of the frontal area of buildings to the total surface area). These  
156 parameters are calculated for each 1 km by 1 km area following the analysis of  
157 Kanda et al. (2013). Figure 3a shows  $\lambda_p$  calculated in the areas of 1 km by 1 km  
158 for the buildings shown in Fig. 2a, with the values of the roughness parameters in  
159 the 1 km by 1 km areas summarized in Fig. 3b. The average values of  $H_{ave}$ ,  $\sigma_H$ ,  
160  $\lambda_p$ , and  $\lambda_f$  over the  $x = 0 - 4$  km region are 10.8, 7, 0.41, and 0.25, respectively,  
161 while the corresponding averages over  $x = 7 - 11$  km are 9.8, 5.3, 0.2, and 0.16,



162 respectively. Thus, the  $x = 0 - 4$  km region is more densely built than the  $x = 7 -$   
 163 11 km. Using building data from Tokyo and Nagoya, Japan, Kanda et al. (2013)  
 164 derived the following empirical relationships between  $\lambda_p$  and  $\lambda_f$ , and between  $H_{ave}$   
 165 and  $\sigma_H$ ,

$$\lambda_f = 1.42\lambda_p^2 + 0.4\lambda_p, \quad (1)$$

$$\sigma_H = 1.05H_{ave} - 3.7. \quad (2)$$

166 Figure 3c and d indicates the respective relationships between  $\lambda_p$  and  $\lambda_f$ , and  
 167 between  $H_{ave}$  and  $\sigma_H$ , based on the data given in Fig. 3b. Also shown in the  
 168 panels are the empirical relationships of Kanda et al. (2013) and the data for North  
 169 American and European cities found in Ratti et al. (2002). For  $\lambda_p > 0.3$ , the  $\lambda_f$   
 170 values for Kyoto tend to be smaller than in the empirical profile. This feature  
 171 of Kyoto appears to be similar to those seen in European cities, and indicates  
 172 that the fraction of high buildings in Kyoto is limited relative to those in major  
 173 metropolitan cities in Japan and North America. The relationship between  $H_{ave}$   
 174 and  $\sigma_H$  for Kyoto is in good agreement with those of Tokyo and Nagoya, but  
 175 differs from those of European cities. Finally, the magnitudes of  $H_{ave}$  and  $\sigma_H$  in  
 176 Kyoto are smaller than those of Los Angeles by a factor of 5 – 10.

177 According to these results, Kyoto can be morphologically characterized as hav-  
 178 ing densely distributed buildings with widely varying heights. The Kyoto dataset  
 179 was used for the numerical simulations described in the next section.

### 180 **3 Numerical Model and Experimental Design**

#### 181 3.1 Numerical Model

182 Our LES model is effectively the same as the one used in Nakayama et al. (2011),  
183 except that it neglects the molecular viscosity term, and employs a bottom bound-  
184 ary condition based on Monin–Obukhov similarity theory, as described later. In  
185 Nakayama et al. (2011), the performance of the LES model reproducing turbu-  
186 lent statistics was validated using data obtained from wind-tunnel experiments;  
187 as a close agreement was found, the model developed by Nakayama et al. (2011)  
188 has subsequently been applied to simulate turbulent flows over actual urban cities.  
189 Nakayama et al. (2012) conducted LES investigations of turbulent flows over Tokyo  
190 by coupling their model with a mesoscale meteorological model, and found that  
191 observed gust factors are accurately reproduced by the model. The model was  
192 also used to successfully reproduce the wind speeds and directions at the ground  
193 level in the Fukushima Daiichi Nuclear Power Plant during the Great East Japan  
194 Earthquake and its aftermath in March 2011 (Nakayama et al., 2015). Nakayama  
195 et al. (2016) further applied their LES model for the simulation of turbulent flows  
196 and plume dispersion over Oklahoma City, and showed that the observed charac-  
197 teristics of turbulence and dispersion are reproduced despite the fact that small  
198 differences in wind direction caused by the building distribution significantly in-  
199 fluenced the plume dispersion. Thus, our LES model has been widely tested and  
200 is applicable for the analysis of the turbulent flow over Kyoto.

201 The LES model solves the filtered continuity and Navier–Stokes equations in  
202 Cartesian coordinates with the subgrid-scale stress parametrized by the standard  
203 Smagorinsky model (Smagorinsky, 1963). The governing equations are

$$\frac{\partial \tilde{u}_i}{\partial x_i} = 0, \quad (3)$$

$$\frac{\partial \tilde{u}_i}{\partial t} + \tilde{u}_j \frac{\partial \tilde{u}_i}{\partial x_j} = -\frac{1}{\rho} \frac{\partial \tilde{p}^*}{\partial x_i} - \frac{\partial \tau_{ij}}{\partial x_j} + f_i, \quad (4)$$

$$\tau_{ij} - \frac{1}{3} \delta_{ij} \tau_{kk} = -2(C_s \Delta)^2 (2\tilde{S}_{ij} \tilde{S}_{ij})^{1/2} \tilde{S}_{ij}, \quad (5)$$

$$\tilde{S}_{ij} = \frac{1}{2} \left( \frac{\partial \tilde{u}_i}{\partial x_j} + \frac{\partial \tilde{u}_j}{\partial x_i} \right), \quad (6)$$

204 where  $t$  denotes time,  $\tilde{u}_i$  is the filtered air velocity in the direction  $i$ ,  $\tilde{p}^* =$   
 205  $\tilde{p} + \frac{1}{3} \rho \tau_{kk}$  is the modified pressure,  $\tilde{p}$  is the filtered pressure,  $\rho$  is the density of air,  
 206  $\tau_{ij}$  is the subgrid-scale stress,  $\delta_{ij}$  is the Kronecker delta,  $\tilde{S}_{ij}$  is the filtered stress  
 207 tensor, and  $f_i$  is the external force exerted by roughness obstacles. The parameter  
 208  $x_i$  represents the coordinate system, with components  $i = 1, 2,$  and  $3$  referring  
 209 to the streamwise ( $x$ ), spanwise ( $y$ ) and vertical ( $z$ ) directions, respectively. In  
 210 addition,  $\Delta = (\Delta_x \Delta_y \Delta_z)^{1/3}$  is the filter width, where  $\Delta_x, \Delta_y,$  and  $\Delta_z$  are the  
 211 streamwise, spanwise, and vertical grid spacings, respectively. The Smagorinsky  
 212 coefficient  $C_s$  is set to 0.14. Note that the viscous term is neglected because our  
 213 target is the simulation of turbulent flow with a high Reynolds number.

214 The external force  $f_i$  is used to simulate the effects of buildings on the flow,  
 215 for which we employ the feedback forcing by Goldstein et al. (1993) who give

$$f_i = \alpha \int_0^t u_i(t') dt' + \beta u_i(t), \quad \alpha < 0, \beta < 0, \quad (7)$$

216 where  $\alpha$  and  $\beta$  are negative constants. The stability limit is given by  $\Delta t <$   
 217  $\frac{-\beta - \sqrt{(\beta^2 - 2\alpha k)}}{\alpha}$ , where  $k$  is a constant of order one. Following Nakayama et al.  
 218 (2011), these constants are set as  $\alpha = -10,$   $\beta = -1,$  and  $k = 1.$

219 The governing equations are discretized on a staggered-grid system. The veloc-  
 220 ity and pressure fields are solved using a coupling method based on the marker-and-

221 cell method (Chorin, 1967). The successive over-relaxation method is used to solve  
222 the Poisson equation for pressure, and the Adams–Bashforth scheme is adopted for  
223 the time integration. A second-order accurate, central-differencing scheme is em-  
224 ployed for spatial discretization. The code is parallelized using a Message Passing  
225 Interface library to reduce the computational time.

### 226 3.2 Experimental Design

227 The governing equations are numerically solved in two computational domains:  
228 the driver region, which features regularly arrayed obstacles, and the main region,  
229 which contains the actual buildings of Kyoto. To ensure the flow field of the LES  
230 is turbulent, a turbulent flow is generated in the driver region and imposed as  
231 the inflow at the boundary of the main region. The concept involved in setting  
232 the driver and the main regions is demonstrated in Fig. 4. The size of the driver  
233 region is 6 km (streamwise)  $\times$  2.4 km (spanwise)  $\times$  1.015 km (vertical), with a  
234 grid spacing of 4 m in the horizontal directions, and a grid spacing stretched with  
235 increasing altitude from 1 m to 16 m in the vertical direction. The total number  
236 of grid points is  $1500 \times 600 \times 105$ . In the driver region, there is one rectangular  
237 block aligned in the spanwise direction, and an array of roughness blocks staggered  
238 with  $\lambda_p = 0.04$ . The individual rectangular and roughness block sizes are  $50 \text{ m} \times$   
239  $2400 \text{ m} \times 50 \text{ m}$  and  $16 \text{ m} \times 16 \text{ m} \times 10 \text{ m}$ , respectively. The purpose of setting  
240 the size of the rectangular block is to enhance perturbations near the inlet of the  
241 driver region. The  $\lambda_p$  value chosen for the block array is set to be a little larger  
242 than that in Nakayama et al. (2014) to reduce the generation of turbulence. The

243 height of the blocks is chosen according to the mean building height in the main  
 244 region.

245 A uniform flow with a velocity magnitude of  $5 \text{ m s}^{-1}$  is imposed at the inflow  
 246 boundary of the driver region. The Sommerfeld radiation condition is imposed at  
 247 the outflow boundary, while a periodic condition is set at the lateral boundaries.  
 248 At the top boundary, free-slip and zero-speed conditions are imposed for the hor-  
 249 izontal and vertical velocity components, respectively. At the ground, a boundary  
 250 condition based on Monin–Obukhov similarity theory is employed. The stress at  
 251 the first vertical grid  $\tau_{i3}(x, y, t)$  is calculated as (Stoll and Porté-Agel, 2006)

$$\tau_{i3}(x, y, t) = - \left[ \frac{\tilde{u}_r(x, y, z_s, t)\kappa}{\ln(z_s/z_0)} \right]^2 \frac{\tilde{u}_i(x, y, z_s, t)}{\tilde{u}_r(x, y, z_s, t)}, \quad (8)$$

252 where  $\tilde{u}_r(x, y, z_s, t) = [\tilde{u}_1(x, y, z_s, t)^2 + \tilde{u}_2(x, y, z_s, t)^2]^{1/2}$  is the instantaneous re-  
 253 solved velocity magnitude,  $z_s$  is the altitude at the first vertical grid,  $z_0$  is the  
 254 roughness length, and  $\kappa$  is the von Kármán constant. Here,  $z_0 = 0.1 \text{ m}$  (Bou-Zeid  
 255 et al., 2009) and  $\kappa = 0.4$ .

256 The ratio of the boundary-layer height  $\delta$  of the generated outflow to the rough-  
 257 ness block height in the driver region is 27.9. Note that, here,  $\delta$  is defined as the  
 258 height at which the mean streamwise velocity component at the outflow indicates a  
 259 peak value. In Nakayama et al. (2011), the ratio of  $\delta$  to the roughness block height  
 260 in the driver region is 13. In addition, we confirmed that the vertical profiles of the  
 261 standard deviation of each velocity component and Reynolds stress are in reason-  
 262 able agreement with those obtained from wind-tunnel experiments, although the  
 263 LES results underestimate the spanwise and vertical components and Reynolds-  
 264 stress values relative to the wind-tunnel results (see Online Resource 1, Figure 1).

265 These results suggest that well-developed, deep turbulent flows are generated in  
266 the driver region.

267 In the main region, the domain size and the total number of grid points are 12  
268 km  $\times$  2.4 km  $\times$  1.015 km and  $3000 \times 600 \times 105$ , respectively. The main region  
269 includes the actual buildings and structures in Kyoto, as shown in Fig. 2a. For  
270 computational purposes, we set a buffer area spanning 500 m and 200 m in the  
271 streamwise and spanwise directions, respectively, surrounding the actual building  
272 area in the main region (not shown in Fig. 2a). The streamwise width of the area  
273 was determined based on Nakayama et al. (2012), who carried out an LES inves-  
274 tigation of the airflow over Tokyo. Whereas Nakayama et al. (2012) did not set a  
275 buffer area in the spanwise direction, we decided that a spanwise buffer is necessary  
276 to avoid building discontinuities arising from the periodic boundary conditions. In  
277 this buffer area, the same roughness blocks used in the driver region are applied to  
278 maintain a turbulent flow over roughness surfaces. Note that the coordinates  $x = 0$   
279 km and  $y = 0$  km are set to the northern and western boundaries, respectively, of  
280 the actual building area in the main region. Correspondingly, the inflow boundary  
281 condition provided by the driver region is set at  $x = -500$  m in the main region.  
282 Outside of the inflow boundary, the boundary conditions of the main region are  
283 the same as those in the driver region, and all grid spacings are identical to those  
284 in the driver region.

285 Hereafter, the simulation using the actual buildings in Kyoto is referred to as  
286 the control experiment (CTL). To reveal the effects of building-height variability,  
287 we conducted an additional experiment referred to as the uniform experiment  
288 (UNI) in which all building heights are set to the average of the actual building  
289 heights in the main region ( $h_{all} = 10.3$  m). The integration time for each of the

two experiments is 7,200 s, with the results obtained from the last 1,800 s used for the analysis of turbulent statistics. In Sect. 4.3, we confirm that the flows were in equilibrium states during this analysis period, as shown Fig. 5. In addition, as seen in Fig. 1 of Online Resource 1, the second-order moments of the inflow profiles are relatively small compared with those of the wind-tunnel experiments, which possibly influences the results presented here. However, as the same inflow condition was applied in both the CTL and UNI experiments, we can assume that any differences in the respective experimental results are unaffected by this issue.

## 4 Comparison with Observations

### 4.1 Observational Setting

The observations were performed at the Ujigawa Open Laboratory of the Disaster Prevention Research Institute, Kyoto University, during the period from 12 January to 12 February 2016. The laboratory is located in the southern part of Kyoto, and is surrounded by low-rise buildings and structures. The location of the observation site is shown in Fig. 1, which includes a meteorological observation tower of height 55 m. This tower is a unique facility first deployed in 1978 (Nakajima et al., 1979), and is currently one of the few meteorological towers operating in Japan.

A sonic anemometer (DA-600, Kaijo Co.) installed on the tower at a 25-m height measures the three velocity components as well as the air temperature at a 10-Hz sampling rate. The surrounding area up to 500 m north of the tower has only low building heights ( $< 25$  m), enabling the assumption that observations taken by the sonic anemometer are not influenced by the strong wakes of tall buildings.

313 We also installed a Doppler lidar (WINDCUBE WLS-7, Leosphere) at the  
 314 ground near the tower, from which we obtained three-component velocity measure-  
 315 ments at heights ranging from 40 m to 200 m with a 20-m interval at a sampling  
 316 rate of 1 Hz.

## 317 4.2 Data Selection

318 The observation site was included in the main region assessed in the numerical  
 319 experiment for the purpose of directly comparing the LES results in the CTL  
 320 experiment with the observations. As the sonic anemometer installed on the tower  
 321 faces northwards, we analyzed data for dominant northerly wind directions to  
 322 minimize the interference from the tower. To extract suitable periods from the  
 323 observational data, we imposed two criteria for sorting values obtained from the  
 324 sonic anemometer. First, a northerly flow condition was adopted by classifying 10-  
 325 min averaged wind directions into 16 classes and extracting periods when northerly  
 326 wind directions ( $348.25^\circ - 360^\circ, 0^\circ - 11.25^\circ$ ) were sustained for at least 30 min.  
 327 Note that the time period for the analysis of the LES data was also 30 min. Second,  
 328 a neutrally stratified condition was chosen based on the Monin–Obukhov stability  
 329 parameter

$$\frac{z}{L} = -\frac{(g/\overline{T})\overline{w'T'}}{u_*^3/\kappa z}, \quad (9)$$

330 so that the assumption of turbulent flows under a neutrally stratified condition in  
 331 the LES model is valid. Here,  $L$  is the Obukhov length (m),  $g$  is the acceleration  
 332 due to gravity ( $\text{m s}^{-2}$ ),  $T$  is the air temperature (K),  $\overline{w'T'}$  is the sensible heat flux  
 333 ( $\text{K m s}^{-1}$ ), and  $u_*$  is the friction velocity ( $\text{m s}^{-1}$ ). An overbar and prime denote



334 a temporal average and fluctuation, respectively. A period for  $|z/L| \leq 0.05$  (Roth,  
335 2000) is regarded as fulfilling the neutrally stratified condition.

336 By imposing the above conditions on the observational data, we obtained the  
337 following four 30-min periods: 0720 – 0750 LT (local time = UTC + 9 h) 22  
338 January; 1650 – 1720 LT 30 January; 0740 – 0810 LT 2 February; and 1830 –  
339 1900 LT 10 February, which are referred to as the D1, D2, D3, and D4 periods,  
340 respectively. The wind directions for each period calculated from the averaged  
341 horizontal velocity components are  $4.9^\circ$ ,  $358.8^\circ$ ,  $353.8^\circ$ , and  $351.5^\circ$  for the D1 to  
342 D4 periods, respectively.

343 To compare the LES results with the observations, it is necessary to use airflows  
344 observed at the Ujigawa Open Laboratory coming from the northern boundary of  
345 the analysis region of Kyoto passing through the analysis region, and not from the  
346 western or eastern boundaries. Because of the periodic conditions at the western  
347 and eastern boundaries, the flow through these lateral boundaries is unlikely to  
348 be accurately simulated by the LES model. This condition requires that wind  
349 directions be within a range of between approximately  $355^\circ$  and  $5^\circ$  based on the  
350 streamwise length and half the spanwise length of the analysis region (i.e.,  $\arctan(1$   
351  $\text{km}/11 \text{ km})$ ). Overall, the wind directions in the periods D1 – D4 are almost  
352 within the range of this condition, although those in the periods D3 and D4 are  
353 slightly shifted westwards from the condition. We confirmed that the area within  
354 at least 1 km westwards from the analysis region is dominated by land-use and  
355 building types similar to those in the analysis region. Thus, we concluded that the  
356 anemometer data taken during the four periods described above are appropriate  
357 for comparison with the LES results. However, the wind directions measure by the  
358 Doppler lidar deviate from those recorded by the sonic anemometer. The directions

359 of the Doppler lidar in the D1 and D3 periods become more westerly with height,  
360 reaching  $330^\circ$  at a height of 200 m, while those in the D2 and D4 periods are  
361 relatively constant with altitude and within a range between approximately  $350^\circ$   
362 and  $0^\circ$ . We discuss the possible influences of the variation of wind direction in  
363 Sect. 4.3. As explained above, none of the observed wind directions were oriented  
364 in a truly northerly fashion. Correspondingly, we rotated the streamwise directions  
365 to the mean of the wind directions measured by the sonic anemometer and the  
366 Doppler lidar.

### 367 4.3 Results

368 Figure 5a and b shows the time series of streamwise and spanwise velocity com-  
369 ponents produced by the LES model and measured by the sonic anemometer at a  
370 25-m height, respectively. To avoid interference from the tower on the wind-speed  
371 profiles, the LES results are shown for a grid point 16 m north of the tower. It  
372 is seen that the LES turbulent fluctuations in both the streamwise and spanwise  
373 directions are quite comparable to those from the anemometer. Note that average  
374 spanwise velocity components are nearly zero, as indicated in Fig. 5b. The stream-  
375 wise velocity component is stronger in the D2 period than in the other periods.  
376 Comparison of the respective weather charts for the four time periods reveals the  
377 stronger wind speeds in the D2 period to be caused by a large low-pressure system  
378 passing through the northwest Pacific Ocean off the coast of the Japanese Islands.

379 Figure 5c shows a comparison of the LES and observed vertical profiles of the  
380 mean streamwise velocity component. Both datasets are averaged over time, and  
381 the time-averaged LES data are averaged horizontally over a 16 m by 16 m area to

the north of the tower to increase the representativeness of the simulated flows for the observation site. Note that, given the logarithmic scales used on both axes, the slopes of the mean streamwise velocity component in Fig. 5c suggest a power-law profile. According to Counihan (1975), the slopes of suburban and urban areas range between 0.21 and 0.28, making a power-law exponent of  $1/4$  suitable for reference, where it is seen that the slopes of the observations and the LES results are very similar to this value. We also examined the respective vertical profiles of the mean streamwise velocity component normalized by the mean streamwise velocity component at the 25-m height (see Online Resource 1, Figure 2) and found that the LES and observed mean streamwise velocity components are quantitatively consistent. We conclude that this result is also good evidence for the reasonable performance of our LES model. In contrast, the slopes above approximately the 150-m height in the D1, D2, and D3 periods appear to deviate from the reference slope. In the case of the D1 and D3 periods, we assume this occurs because of the change in wind direction from northerly to westerly, as described in the previous subsection. Another possible explanation for the deviation at the higher levels is that the stability conditions may not have been neutral at these heights during the observed periods. Because there were no observational data available to classify the stability condition above height of the sonic anemometer at 25 m, it is impossible to quantitatively reveal the stability above that height.

The vertical profiles of Reynolds stress in both the observations and the LES results are shown in Fig. 5d. Note that the Reynolds stress is normalized by the mean streamwise velocity components at each height. The Reynolds stress of the LES data is averaged horizontally over the same 16 m by 16 m area used for the mean streamwise velocity component. It is seen that the vertical profile of the LES

407 data is within the range of differences found in the observation periods, which is a  
408 feature similar to that of the profiles normalized by the mean streamwise velocity  
409 component at the 25-m height (see Online Resource 1, Figure 2). However, it is  
410 necessary to be careful in comparing the LES results with the Doppler lidar data  
411 because the latter might include some errors in representing perturbations of the  
412 wind speed as discussed below.

413 We now compare the results for the turbulence intensity, which is the ratio  
414 of the standard deviation of each velocity component  $\sigma_i$  to the mean streamwise  
415 velocity component. As previously mentioned, the turbulence intensity was also  
416 averaged horizontally in the 16 m by 16 m area. Figure 6 compares the vertical  
417 profiles of turbulence intensity in the LES results and observations with the em-  
418 pirical form of the ESDU (1985), which is a database providing the turbulence  
419 characteristics of a neutrally stratified atmospheric boundary layer based on var-  
420 ious field measurements from around the world. In Fig. 6, all sonic-anemometer  
421 components fall within the rough-surface category given by the ESDU, which in-  
422 dicates suburban areas with  $z_0$  between 0.1 and 0.5. Each component simulated  
423 by the LES model appears to capture the vertical distribution of that obtained by  
424 the ESDU within or around its upper and lower limits, at least below about the  
425 height of 150 m, while being slightly smaller than those of the sonic-anemometer  
426 observations. In fact, the values obtained from the sonic anemometer lie near the  
427 upper limit of the ESDU profile, suggesting that the LES results within the ESDU  
428 range are generally more favourable.

429 In contrast, there appears to be large discrepancies between the Doppler lidar  
430 observations and the LES results in terms of the  $u$  and  $v$  velocity components.  
431 The turbulence intensities for these components measured by the Doppler lidar

432 are even larger than the upper limits of the ESDU, suggesting that the measure-  
433 ments may include an overestimating bias for the turbulence intensities. It is in  
434 fact commonly understood that the Doppler lidar measurements overestimate the  
435 turbulence intensities for the streamwise component. This characteristic was noted  
436 in Cañadillas et al. (2011), who showed that the results produced by the Doppler  
437 lidar observations are larger than those of sonic anemometers at various wind  
438 speeds and altitudes, and the deviations become larger with the decrease in wind  
439 speed. A close look at Figs. 5c and Fig. 6a indicates that the difference between  
440 Doppler lidar and the ESDU in terms of the streamwise turbulence intensity be-  
441 low 100 m decreases as the streamwise velocity component increases, in apparent  
442 confirmation of the finding of Cañadillas et al. (2011). For the Doppler lidar data  
443 above 100 m, changes in the wind direction and uncertainty in the stability, as  
444 revealed in the mean streamwise velocity component, may contribute to this over-  
445 estimation. An overestimating tendency in the lidar data can also be found for the  
446 spanwise component, which has a mean value of nearly zero.

447 The vertical component produced by the LES results appears to be consistent  
448 with both the lidar data and the ESDU profile, but the lidar tends to underestimate  
449 the vertical turbulence intensity, particularly in weaker wind-speed conditions.

450 Figure 7 shows the power spectra of the time series of each velocity component  
451 obtained from the LES results and the sonic anemometer at a height of 25 m. The  
452 spectra were calculated from the time series shown in Fig. 5, and the frequency  
453  $f$  and velocity spectra  $E(f)$  are normalized in dimensionless form. The figure  
454 includes the empirical reference from Kaimal et al. (1972) derived from observa-  
455 tions over a rural region. A close agreement is seen between the sonic anemometer  
456 and the reference results for all three components. The spectra from the sonic

457 anemometer clearly represent an inertial subrange with a  $2/3$  slope. Comparison  
458 of the LES spectra with the observations and empirical reference reveals that the  
459 spectra of the  $u$  and  $v$  components of the LES data are similar to those of the sonic  
460 anemometer data except in the highest frequency range. The lower frequency por-  
461 tion of the inertial subrange appears to be well reproduced for these components  
462 in the LES results.

463 However, the LES model is able to reproduce the vertical velocity components  
464 in only the lowest frequency portion of the inertial subrange. It is possible that  
465 the grid spacing used in our modelling is insufficient for resolving the smallest  
466 eddies and their corresponding vertical motion. Further increases in the vertical  
467 resolution may be required to represent the small-scale vertical motion likely to be  
468 induced at the edges of buildings. However, we note that the spectral peak of the  
469  $w$  component in the LES results agrees well with that of the sonic anemometer.

470 From the above comparisons, we conclude that the use of our LES model leads  
471 to a reasonable reproduction of the turbulent boundary-layer flow over actual  
472 buildings under a neutral stability condition, at least up to a height of about 150  
473 m. We emphasize that, in general, the results produced by our LES model agree  
474 favourably with the observations within the range of differences among the chosen  
475 periods (D1 – D4), even though our inflow condition employed an idealized turbu-  
476 lent flow generated in the driver region without realistic meteorological conditions.  
477 These results are sufficient here because our analysis of building-height variabil-  
478 ity focuses on altitudes below approximately 25 m (i.e., at height  $z = 2.5h_{all}$ ),  
479 where the LES results show an especially close agreement with the observations,  
480 as shown in Figs. 6 and 7.

## 481 5 Sensitivity to Building-Height Variability

### 482 5.1 General characteristics of turbulent flows

483 We now focus on the overall characteristics of turbulent flows in the CTL and UNI  
484 experiments, starting with the differences between the respective experiments.

485 Figure 8a and b shows the vertical profiles of the space- and time-averaged  
486 streamwise velocity component  $\langle \bar{u} \rangle_{all}$  and Reynolds stress  $-\langle \overline{u'w'} \rangle_{all}$  over  
487 the entire main region for the CTL and UNI experiments, respectively. Here, the  
488 angled brackets denote a spatial average, while the subscript *all* refers to the overall  
489 main region. Note that the values are normalized by the mean streamwise velocity  
490 component  $U_\infty$  at the height of the boundary-layer ( $\delta$ ). The mean streamwise ve-  
491 locity components above height  $z = h_{all}$  (i.e., above the canopy layer) are lower in  
492 the CTL experiment than in the UNI experiment. In contrast, the velocities below  
493 height  $z = h_{all}$  for the CTL experiment are higher than in the UNI experiment.  
494 The Reynolds stress above height  $z = h_{all}$  in the CTL experiment is larger than  
495 that in UNI experiment. Furthermore, the level of peak Reynolds stress is higher  
496 in the CTL experiment than in the UNI experiment.

497 These differences between the CTL and UNI results can be attributed to the  
498 effects of building-height variability. Using the LES results of flows over idealized  
499 arrays of roughness blocks, Nakayama et al. (2011) showed that the mean velocity  
500 above the building height decreases with increasing building-height variability, and  
501 that the magnitude and height of the peak of the Reynolds stress both increase  
502 with building-height variability. Our results in terms of the streamwise velocity  
503 component and Reynolds stress are consistent with the results of Nakayama et al.  
504 (2011).

505 Xie et al. (2008) carried out an LES investigation over block arrays with ran-  
 506 dom and uniform heights, and found that both types of arrays produced similar  
 507 turbulent kinetic energies below the average building height. The Reynolds stresses  
 508 produced in the CTL and UNI experiments below height  $z = h_{all}$  are consistent  
 509 with their results. From Fig. 8b, it is seen that the Reynolds stress in the UNI  
 510 experiment sharply increases around height  $z = h_{all}$ , which is likely caused by  
 511 the presence of the uniform tops of buildings in the UNI experiment, resulting in  
 512 sharp wind shear and the generation of turbulence.

513 In Coceal et al. (2006), the velocity components  $u_i$  were decomposed as

$$u_i = \langle \bar{u}_i \rangle + \bar{u}_i'' + u_i', \quad (10)$$

514 where  $\langle \bar{u}_i \rangle$  are the time- and space-averaged velocities,  $\bar{u}_i''$  is the spatial vari-  
 515 ation of the time-averaged velocity, and  $u_i'$  is the turbulent fluctuation. Coceal  
 516 et al. (2006) showed that dispersive flux, which is defined as  $\langle \bar{u}'' \bar{w}'' \rangle$ , signifi-  
 517 cantly contributes to the total momentum flux in the canopy layer in which the  
 518 time-averaged velocities are spatially inhomogeneous. The vertical profiles of the  
 519 dispersive flux normalized by  $U_\infty$  in the CTL and UNI experiments are shown  
 520 in Fig. 8c. Although the dispersive fluxes for both experiments have peaks just  
 521 below height  $z = h_{all}$ , the magnitude of the peak in the UNI experiment is larger  
 522 than that in the CTL experiment. The UNI profile decreases sharply with height  
 523 above the height of the peak. Above height  $z = h_{all}$ , the dispersive flux in the  
 524 CTL experiment is larger than that in the UNI experiment up to about height  
 525  $z = 3.5h_{all}$ . Xie et al. (2008) performed an LES investigation to compare the  
 526 dispersive flux in random and uniform block arrays. Their results suggest that  
 527 both types of dispersive flux have peaks near the average building height, that



528 the peaks obtained from uniform block arrays are stronger than those for random  
 529 block arrays, and that the dispersive flux of uniform block arrays decreases much  
 530 more abruptly with increasing height above the height of the peak than that of  
 531 random block arrays. These characteristics are qualitatively consistent with our  
 532 results. The dispersive fluxes in both the CTL and UNI experiments appear not to  
 533 decrease linearly with height because the time-averaged velocities are not spatially  
 534 homogeneous at heights above the canopy layer. Based on the results shown in Fig.  
 535 8a and b, we focus on the height of  $z = 0.5h_{all}$  at which the difference between  
 536 the CTL and UNI experiments is small, and the height of  $z = 2.5h_{all}$  where clear  
 537 differences are seen between the respective experiments.

538 Figure 9 shows the fields of time-averaged streamwise velocity component nor-  
 539 malized by  $U_\infty$  for the CTL and UNI experiments over an upstream region ( $x =$   
 540  $1 - 5$  km) in which the business districts are located. The difference between  
 541 the respective experimental results for the region appears to be small at height  
 542  $z = 0.5h_{all}$  except in areas along a major street around  $y = 1.3$  km. This is likely  
 543 caused by a stronger convergence of the streamwise velocity components on the  
 544 street in the UNI experiment owing to enhancements arising from the presence of  
 545 uniform-height buildings (i.e., in the UNI experiment, all lower building heights are  
 546 raised to  $z = h_{all}$ ). The velocity-deficit regions are reproduced at height  $z = 2.5h_{all}$   
 547 behind buildings in the CTL experiment, which contrasts to the smooth field of  
 548 time-averaged streamwise velocity components at height  $z = 2.5h_{all}$  in the UNI  
 549 experiment.

550 Figure 10 shows the fields of Reynolds stress normalized by  $U_\infty$  for the CTL  
 551 and UNI experiments over the upstream region. While the features are quite similar  
 552 at height  $z = 0.5h_{all}$ , the field at height  $z = 2.5h_{all}$  in the CTL results has larger

553 values behind the buildings than in the UNI results, which indicates the important  
554 role of sparsely and randomly distributed buildings at and above height  $z = 2.5h_{all}$   
555 in generating turbulence in the CTL experiment.

## 556 5.2 Analysis of Roughness Parameter

557 To quantitatively reveal the effects of building-height variability, we examined the  
558 relationships between the turbulent statistics and roughness parameters. The plan-  
559 area index  $\lambda_p$  is used for this analysis because the CTL and UNI experiments have  
560 the same values for this parameter. Turbulent statistics were derived in each 1 km  
561 by 1 km area in a manner similar to that used to find the roughness parameters  
562 in Sect. 2.

### 563 5.2.1 Reynolds stress

564 Figure 11 shows how the Reynolds stress normalized by  $U_\infty$  in the CTL and  
565 UNI experiments changes as a function of  $\lambda_p$  at the heights of  $z = 0.5h_{all}$  and  
566  $z = 2.5h_{all}$ . The brackets with subscript  $1 \text{ km}^2$  indicate spatial averaging over a 1  
567 km by 1 km area. The Reynolds stress at height  $z = 0.5h_{all}$  is very similar for the  
568 two experiments, which is consistent with the features shown in Fig. 10a and b.  
569 By contrast, the values at height  $z = 2.5h_{all}$  in the CTL experiment increase with  
570  $\lambda_p$ , while those in the UNI experiment are nearly independent of  $\lambda_p$ . In addition,  
571 the differences between the CTL and UNI results at height  $z = 2.5h_{all}$  are more  
572 apparent when  $\lambda_p > 0.32$ .

573 As shown in Figs. 9 and 10, the difference between the CTL and UNI exper-  
574 iments in terms of building distributions at height  $z = 2.5h_{all}$  has a significant

575 effect on the turbulent flow results. To interpret this difference, we calculated the  
 576 respective plan-area indices  $\lambda_p$  at this altitude; i.e., for each experiment, if the  
 577 building height in a grid cell is below  $z = 2.5h_{all}$ , the grid cell is regarded as  
 578 having no buildings. Figure 12a and b shows  $\lambda_p$  at heights  $z = 0.5h_{all}$  (denoted  
 579 by  $\lambda_{p, 0.5h_{all}}$ ) and  $z = 2.5h_{all}$  ( $\lambda_{p, 2.5h_{all}}$ ), respectively, plotted against  $\lambda_p$  at the  
 580 surface for both the CTL and UNI experiments. Note that, in the UNI experiment,  
 581 the value of  $\lambda_{p, 0.5h_{all}}$  is the same as that of  $\lambda_p$  at the surface, and that  $\lambda_{p, 2.5h_{all}}$   
 582 is zero for this experiment. The difference between the CTL and UNI experiments  
 583 in terms of  $\lambda_{p, 0.5h_{all}}$  is not very large, confirming the similarity of the respec-  
 584 tive Reynolds stresses at height  $z = 0.5h_{all}$  in Fig. 10. In the CTL experiment,  
 585  $\lambda_{p, 2.5h_{all}}$  rapidly increases if  $\lambda_p$  exceeds 0.32, which appears to be consistent with  
 586 the Reynolds-stress feature in the CTL experiment at height  $z = 2.5h_{all}$  as seen  
 587 in Fig. 10. Based on these results, we suggest that the Reynolds stress from the  
 588 CTL experiment at height  $z = 2.5h_{all}$  becomes stronger at  $\lambda_p > 0.32$  because  
 589 some building clusters are still present at height  $z = 2.5h_{all}$  in this experiment.

590 The frontal-area index  $\lambda_f$  is another important parameter for describing the ge-  
 591 ometrical characteristics of urban areas. Here we examine the frontal area of build-  
 592 ings above the height  $h_{all}$ . Figure 12c shows  $\lambda_f$  above height  $z = h_{all}$  ( $\lambda_{f, h_{all}}$ )  
 593 plotted against  $\lambda_p$  for the CTL experiment (the figure does not include the corre-  
 594 sponding values for the UNI experiment owing to the absence of buildings at that  
 595 altitude). It is seen that  $\lambda_{f, h_{all}}$  increases with  $\lambda_p$ , and sharply increases when  
 596  $\lambda_p > 0.32$ . These features agree well with the characteristics determined above  
 597 for  $\lambda_{p, 2.5h_{all}}$  and the Reynolds stress. According to these results, the effects of  
 598 building-height variability on the Reynolds stress increase with  $\lambda_p$  when  $\lambda_p$  is

599 greater than 0.32, and are closely linked to the higher values of  $\lambda_p$ ,  $2.5h_{all}$  and  
600  $\lambda_f$ ,  $h_{all}$  at such values of  $\lambda_p$ .

601 Interestingly, Zaki et al. (2011) found that the drag coefficient  $C_d$  in wind-  
602 tunnel experiments, which is relevant to the Reynolds stress, increases with  $\lambda_p$   
603 when  $\lambda_p > 0.32$  in flows over block arrays with random heights. A similar feature  
604 can also be found for the Reynolds stress and  $C_d$  in the LES investigation by  
605 Nakayama et al. (2011). According to Zaki et al. (2011), this is because taller  
606 buildings, which contribute largely to the total drag in a block array (Xie et al.,  
607 2008), tend to be sparsely distributed and, therefore, despite the increase in  $\lambda_p$ ,  
608 the flow pattern does not enter a skimming flow regime (Oke, 1988). Based on  
609 these previous studies and our results,  $\lambda_p \approx 0.3$  can be regarded as a threshold  
610 at which the effects of building-height variability on the turbulent flow become  
611 apparent in various cities.

### 612 5.2.2 Momentum transfer according to a quadrant analysis

613 As described in Sect. 1, turbulent coherent structures over urban surfaces are re-  
614 lated to the physical process of turbulent momentum transfer. A quadrant analysis  
615 is a useful method for identifying the characteristics of the momentum transfer as-  
616 sociated with coherent structures, and has been used in numerous studies of wall  
617 turbulence (Wallace, 2016). This method divides the Reynolds stress into four  
618 components based on the signs of  $u'$  and  $w'$ : outwards interaction (quadrant 1,  
619  $u' > 0$ ,  $w' > 0$ ); ejection (quadrant 2,  $u' < 0$ ,  $w' > 0$ ); inwards interaction  
620 (quadrant 3,  $u' < 0$ ,  $w' < 0$ ) and sweep (quadrant 4,  $u' > 0$ ,  $w' < 0$ ). Raupach  
621 (1981) introduced a conditional averaging using the threshold  $H$  to investigate the

622 contribution to the Reynolds stress from the  $i$ th quadrant as

$$\langle u'w' \rangle_{i, H} = \lim_{T \rightarrow \infty} \frac{1}{T} \int_0^T u'(t)w'(t)I_{i, H}[u'(t), w'(t)]dt, \quad (11)$$

623 where the trigger indicator  $I_{i, H}$  is defined as

$$I_{i, H}(u', w') = \begin{cases} 1, & \text{if } (u', w') \text{ is in quadrant } i \text{ and if } |u'w'| \geq H|\overline{u'w'}|, \\ 0, & \text{otherwise.} \end{cases} \quad (12)$$

624 The fraction of stress exceeding the threshold, which indicates the relative quantity

625 of the  $i$ th quadrant, is

$$S_{i, H} = \langle u'w' \rangle_{i, H} / \overline{u'w'}. \quad (13)$$

626 It is noted that the relationship

$$S_{1, 0} + S_{2, 0} + S_{3, 0} + S_{4, 0} = 1 \quad (14)$$

627 holds only for  $H = 0$ . When the Reynolds stress is negative (as is normally seen in

628 the boundary layer),  $S_{2, 0}$  and  $S_{4, 0}$  are positive, while  $S_{1, 0}$  and  $S_{3, 0}$  are negative.

629 Ejections and sweeps contribute to the downwards momentum flux, and are  
630 considered to be associated with organized turbulent motions as indicated in Sect.

631 1. Thus, the magnitude of ejections and sweeps is a good indicator for determining

632 the characteristics of turbulent flows.

633 To further reveal the relative roles of ejections and sweeps in vertical momen-  
634 tum transfer, we introduce the two parameters

$$\Delta S_0 = S_{4,0} - S_{2,0}, \quad (15)$$

$$Ex = (S_{1,0} + S_{3,0}) / (S_{2,0} + S_{4,0}), \quad (16)$$

635 where  $\Delta S_0$  is the difference between sweeps and ejections, and  $Ex$ , which is called

636 the exuberance (Shaw et al., 1983), is the ratio of unorganized ( $S_1$  and  $S_3$ ) mo-

637 tions to organized ( $S_2$  and  $S_4$ ) motions. The exuberance indicates the efficiency

638 of the vertical momentum flux. Christen et al. (2007) used these parameters to  
639 investigate vertical momentum exchange in an urban district and elucidated the  
640 roles of coherent structures in momentum transport.

641 Figure 13 shows the vertical profiles of  $\Delta S_0$  and  $Ex$  for the CTL and UNI  
642 experiments, which are averaged temporally and spatially in a manner similar to  
643 the profiles in Fig. 8, where  $\Delta S_0$  in the CTL experiment is generally larger than in  
644 the UNI experiment, except for heights around  $h_{all}$ . This feature of  $\Delta S_0$  contrasts  
645 to the vertical profile of the Reynolds stress shown in Fig. 8b, which indicates that  
646 the Reynolds stress is nearly identical in the CTL and UNI experiments below  
647 height  $z = 0.5h_{all}$ . This suggests that, despite the similarities in the Reynolds  
648 stress seen in the two experiments, the building-height variability in the CTL  
649 experiment changes the ratio of ejections to sweeps within the building canopy  
650 layer. In the upper layer from heights  $z = 2.5h_{all}$  to  $z = 10h_{all}$ , both  $\Delta S_0$  and the  
651 Reynolds stress are larger in the CTL experiment than in the UNI experiment.  
652 We consider that the increased Reynolds stress in this upper layer in the CTL  
653 experiment is caused by a sweep-dominated vertical flux.

654 Figure 13b shows the value of  $Ex$  below  $z = 2.5h_{all}$  in the CTL experiment  
655 to be smaller than that in the UNI experiment. Below  $z = 0.5h_{all}$ , the decrease  
656 in  $Ex$  appears to be more pronounced in the CTL experiment than in the UNI  
657 experiment even though the respective Reynolds stresses are similar, as shown in  
658 Fig. 8b. This indicates that the efficiency of the vertical momentum flux in the  
659 canopy layer is reduced by building-height variability. In contrast, the values of  
660  $Ex$  in the CTL and UNI experiments are very similar at altitudes above height  
661  $z = 2.5h_{all}$ , indicating that the efficiency of the momentum flux above these  
662 altitudes is similar for both experiments.

663 Based on the differences between the vertical profiles shown in Fig. 13, we  
 664 focus on the heights  $z = 0.5h_{all}$  and  $z = 2.5h_{all}$  to reveal the relationship between  
 665 building-height variability and turbulent-flow characteristics. Figure 14a and b  
 666 shows variations in  $\Delta S_0$  against  $\lambda_p$  in the CTL and UNI experiments at these two  
 667 altitudes. At height  $z = 0.5h_{all}$ , sweeps are dominant among the contributions  
 668 to the Reynolds stress for both experiments, which is consistent with previous  
 669 results showing a stronger contribution of sweeps to the total momentum flux  
 670 than ejections near and below the tops of block arrays (Raupach 1981; Coceal  
 671 et al. 2007a). From Fig. 13a, it is seen that the contribution of sweeps in the  
 672 CTL experiment is larger than in the UNI experiment. By contrast, the value of  
 673  $\Delta S_0$  at height  $z = 0.5h_{all}$  appears to be independent of  $\lambda_p$  in both experiments.  
 674 However, at height  $z = 2.5h_{all}$ , the value of  $\Delta S_0$  in the CTL experiment increases  
 675 with  $\lambda_p$  when  $\lambda_p > 0.32$ , while in the UNI experiment, it is independent of  $\lambda_p$ .  
 676 The increase in  $\Delta S_0$  in the CTL experiment is consistent with the Reynolds-stress  
 677 results shown Fig. 11b, thus suggesting that sweeps contribute to the increase in  
 678 Reynolds stress for  $\lambda_p > 0.32$ . Similar results were noted by Kanda (2006).

679 Figure 14c and d shows  $Ex$  plotted against  $\lambda_p$  in the CTL and UNI experiments  
 680 at heights  $z = 0.5$  and  $2.5h_{all}$ , respectively, where the difference in the value of  $Ex$   
 681 at height  $z = 0.5h_{all}$  increases with  $\lambda_p$ , suggesting the dominance of unorganized  
 682 structures as  $\lambda_p$  increases. As shown in Fig. 13b, at height  $z = 2.5h_{all}$  the values  
 683 of  $Ex$  in both experiments are practically independent of  $\lambda_p$ .

684 By setting  $H$  in Eq. 12 to a value larger than zero, we evaluate the extent to  
 685 which extreme instantaneous momentum fluxes contribute to the total Reynolds  
 686 stress in a certain period. We define the percentage contribution to the Reynolds  
 687 stress of a value of  $u'w'$  larger than the Reynolds stress by a factor of  $H$  using

$$E_H \equiv \sum_{i=1}^4 S_{i, H} = \sum_{i=1}^4 \langle u'w' \rangle_{i, H} / \overline{u'w'}. \quad (17)$$

688 Unlike in Raupach (1981) in which each component of the momentum flux was  
 689 evaluated, all of the components in Eq. 17 are added to assess the total of the  
 690 extreme momentum fluxes. We set  $H = 20$  here to extract extreme values of  $u'w'$ ,  
 691 with qualitatively similar results also found with  $H = 15$  and  $H = 10$ . Thus,  $H =$   
 692  $20$  is assumed to be a representative value.

693 Figure 14e and f shows the variations of  $E_{20}$  with  $\lambda_p$  at heights  $z = 0.5$  and  
 694  $z = 2.5h_{all}$ , respectively, for both experiments. The results at height  $z = 0.5h_{all}$   
 695 reveal small differences between the CTL and UNI experiments and are, in general,  
 696 larger than those at height  $z = 2.5h_{all}$ . This indicates that the flow is highly  
 697 turbulent at height  $z = 0.5h_{all}$ , and that the extreme values of the momentum  
 698 flux contribute more significantly to the total momentum flux at this altitude.  
 699 However, as the magnitude of  $u'w'$  itself is low at height  $z = 0.5h_{all}$ , the effects of  
 700 the fluctuation itself may not be very strong. It is seen that, at height  $z = 2.5h_{all}$ ,  
 701 the value of  $E_{20}$  in the CTL experiment increases with  $\lambda_p$ , but is independent of  
 702  $\lambda_p$  in the UNI experiment. Moreover, the shape of the relationship between  $E_{20}$   
 703 at height  $z = 2.5h_{all}$  and  $\lambda_p$  in the CTL experiment appears to be quite similar to  
 704 that between  $\lambda_{p, 2.5h_{all}}$  and  $\lambda_p$  shown in Fig. 12b. This suggests that increasing  
 705 the number of buildings at height  $z = 2.5h_{all}$  generates highly turbulent flows at  
 706 higher values of  $\lambda_p$ .

707 The increase in the contribution from extreme values of  $u'w'$  to the Reynolds  
 708 stress at height  $z = 2.5h_{all}$  in the CTL experiment occurs because the building-  
 709 height variability in this experiment leads to a higher momentum flux at this



710 altitude as clearly indicated in Fig. 15a, which shows the horizontal cross-section  
711 of  $E_{20}$  over a 1 km by 1 km area within one of the business districts. It is seen  
712 that high values of  $E_{20}$  appear in areas around randomly and sparsely distributed  
713 buildings. In contrast, areas with higher  $E_{20}$  values also correspond to areas with a  
714 weak Reynolds stress and small value of  $Ex$  (see Fig. 15b and c), which indicates  
715 the small contribution of the extreme momentum flux around buildings to the  
716 total momentum flux, and is not related to organized turbulent motion. From  
717 the features demonstrated in Figs. 14 and 15, it is seen that the turbulent flow  
718 characteristics and contributions of extreme momentum fluxes are significantly  
719 influenced by the presence of buildings with significant height variability.

720 We have shown the qualitative consistency of the Reynolds stress and quadrant  
721 analysis results, if averaged both in time and space, with that over block arrays  
722 with variable height. In contrast, the inhomogeneous profiles of the turbulent-flow  
723 characteristics (Fig. 15) suggest that the local characteristics of the turbulent flow  
724 over urban surfaces are significantly influenced by the inhomogeneity of actual  
725 urban buildings, and would not be expected to be similar to that over idealized  
726 block arrays.

## 727 **6 Summary and Conclusions**

728 An LES investigation of the turbulent flow over the city of Kyoto has been con-  
729 ducted to investigate the effects of building-height variability on the turbulence  
730 in the lower part of the urban boundary layer. A digital surface model data has  
731 reproduced the actual buildings of Kyoto in the LES model.

732 We used roughness parameters such as  $H_{ave}$ ,  $\sigma_H$ ,  $\lambda_p$ , and  $\lambda_f$  to evaluate the  
733 morphological characteristics of buildings, and compared these parameters with  
734 those derived for Tokyo, Nagoya as well as for North American and European  
735 cities. For  $\lambda_p > 0.3$ , the value of  $\lambda_f$  for Kyoto is small compared with the em-  
736 pirical values for Tokyo and Nagoya, but similar to those obtained for European  
737 cities. The relationship between  $H_{ave}$  and  $\sigma_H$  in Kyoto agrees closely with the em-  
738 pirical profile. From these comparisons, the building morphological characteristics  
739 of Kyoto indicate a dense distribution, and buildings with a variety of heights.

740 We compared the LES results with observations of atmospheric turbulence  
741 obtained using a sonic anemometer and a Doppler lidar at the Ujigawa Open  
742 Laboratory, which is an area included in the main region of the LES model. For  
743 this comparison, certain periods were extracted from the total set of observations to  
744 meet the weather conditions assumed in the LES model. The model is to reproduce  
745 the observed characteristics of turbulence up to a height of about 150 m.

746 We carried out two experiments: one modelling the actual buildings of Kyoto  
747 (CTL), and one (UNI) in which all building heights were set to the average building  
748 height in the main region of the city  $h_{all}$ . We find small differences between the  
749 CTL and UNI experiments in terms of the mean streamwise velocity component  
750 and the Reynolds stress at height  $z = 0.5h_{all}$ , but large differences at height  
751  $z = 2.5h_{all}$ . The spatial fields of time-averaged streamwise velocity components  
752 and Reynolds stresses produced in the CTL experiment indicate regions of reduced  
753 velocity and strong Reynolds stress behind sparsely and randomly distributed  
754 buildings at height  $z = 2.5h_{all}$ ; this contrasts with the UNI results, in which  
755 these fields at height  $z = 2.5h_{all}$  are smooth. We investigated the relationships  
756 between turbulent statistics and  $\lambda_p$  evaluated over 1 km by 1 km areas to reveal

757 the differences between the CTL and UNI experiments. The Reynolds stress in the  
758 CTL experiment at height  $z = 2.5h_{all}$  is larger than that in the UNI experiment  
759 when  $\lambda_p > 0.32$ , while the Reynolds stress at height  $z = 0.5h_{all}$  is similar for  
760 both experiments. We suggest that the increase in the Reynolds stress at height  
761  $z = 2.5h_{all}$  is caused by the presence of some building clusters at height  $z = 2.5h_{all}$   
762 in the CTL experiment, and that a value of  $\lambda_p$  of about 0.3 is the threshold above  
763 which the effects of building-height variability become obvious over various urban  
764 surfaces.

765 A quadrant analysis was used to investigate the characteristics of turbulent  
766 coherent flows. Sweeps in the CTL experiment at height  $z = 2.5h_{all}$  are found  
767 to increase with  $\lambda_p$  for  $\lambda_p > 0.32$ , which is similar to that seen in the Reynolds  
768 stress for  $\lambda_p > 0.32$ , suggesting the increase in Reynolds stress is caused by the  
769 presence of sweeps. The vertical momentum flux in the CTL experiment is less  
770 efficient than that in the UNI experiment at height  $z = 0.5h_{all}$ , which indicates  
771 that the building-height variability in the CTL experiment reduces the efficiency  
772 of the flux in the canopy layer.

773 The contributions of the extreme instantaneous momentum flux to the total  
774 Reynolds stress were also investigated. The amount of extreme momentum flux  
775 in the CTL experiment at height  $z = 2.5h_{all}$  depends strongly on the presence  
776 of buildings at this altitude. Examination of horizontal cross-sections reveals that  
777 areas with extreme momentum fluxes are distributed around buildings. However,  
778 the efficiency of the Reynolds stress and momentum flux are small in areas with  
779 an extreme momentum flux, implying its negligible contribution around build-  
780 ings to the net Reynolds stress, as well as the lack of association with coherent  
781 turbulent motions. The relationships between turbulent coherent structures and

782 building-height variability were investigated through the use of space- and time-  
783 averaged profiles. However, future research on turbulent coherent structures over  
784 urban surfaces should focus on instantaneous and local structures, such as vortex  
785 structures behind high, isolated buildings (Park et al., 2015), and flow patterns  
786 in block arrays associated with coherent structures above blocks (Inagaki et al.,  
787 2012).

788 **Acknowledgements** We would like to thank the editor and three anonymous reviewers for  
789 their helpful comments and suggestions. We would like to express our deepest gratitude to  
790 Dr. Wim Vanderbauwhede at the University of Glasgow, who helped to create an MPI version  
791 of the code. We thank Dr. Hiromasa Nakayama at the Japan Atomic Energy Agency for his  
792 guidance on the LES modelling. We would like to thank the support by Prof. Hajime Nakagawa  
793 of Kyoto University for conducting the field measurements at the Ujigawa Open Laboratory.  
794 This research partly used computational resources under the Collaborative Research Program  
795 for Young Scientists provided by the Academic Centre for Computing and Media Studies,  
796 Kyoto University. This study was supported by JSPS Kakenhi grant numbers 26282107 and  
797 16H01846, and DPRI Collaborative Research 28H-04 and 29S-01.

## 798 **References**

- 799 Bou-Zeid E, Overney J, Rogers BD, Parlange MB (2009) The effects of build-  
800 ing representation and clustering in large-eddy simulations of flows in urban  
801 canopies. *Boundary-Layer Meteorol* 132(3):415–436
- 802 Cañadillas B, Westerhellweg A, Neumann T (2011) Testing the performance of  
803 a ground-based wind lidar system: One year intercomparison at the offshore  
804 platform fino1. *Dewi Mag* 38:58–64

- 805 Cheng H, Castro IP (2002) Near wall flow over urban-like roughness. *Boundary-*  
806 *Layer Meteorol* 104(2):229–259
- 807 Chorin AJ (1967) A numerical method for solving incompressible viscous flow  
808 problems. *J Comput Phys* 2(1):12–26
- 809 Christen A, van Gorsel E, Vogt R (2007) Coherent structures in urban roughness  
810 sublayer turbulence. *Int J Climatol* 27(14):1955–1968
- 811 Coceal O, Thomas T, Castro I, Belcher S (2006) Mean flow and turbulence  
812 statistics over groups of urban-like cubical obstacles. *Boundary-Layer Meteoro-*  
813 *rol* 121(3):491–519
- 814 Coceal O, Dobre A, Thomas T, Belcher S (2007a) Structure of turbulent flow over  
815 regular arrays of cubical roughness. *J Fluid Mech* 589:375–409
- 816 Coceal O, Dobre A, Thomas TG (2007b) Unsteady dynamics and organized struc-  
817 tures from dns over an idealized building canopy. *Int J Climatol* 27(14):1943–  
818 1953
- 819 Counihan J (1975) Adiabatic atmospheric boundary layers: a review and analysis  
820 of data from the period 1880–1972. *Atmos Environ* 9(10):871–905
- 821 ESDU (1985) Characteristics of atmospheric turbulence near the ground. part ii:  
822 single point data for strong winds (neutral atmosphere). ESDU International,  
823 London
- 824 Giometto M, Christen A, Meneveau C, Fang J, Krafczyk M, Parlange M (2016)  
825 Spatial characteristics of roughness sublayer mean flow and turbulence over a  
826 realistic urban surface. *Boundary-Layer Meteorol* 160(3):425–452
- 827 Goldstein D, Handler R, Sirovich L (1993) Modeling a no-slip flow boundary with  
828 an external force field. *J Comput Phys* 105(2):354–366

- 829 Inagaki A, Castillo MCL, Yamashita Y, Kanda M, Takimoto H (2012) Large-eddy  
830 simulation of coherent flow structures within a cubical canopy. *Boundary-Layer*  
831 *Meteorol* 142(2):207–222
- 832 Kaimal J, Wyngaard J, Izumi Y, Coté O (1972) Spectral characteristics of surface-  
833 layer turbulence. *Q J R Meteorol Soc* 98(417):563–589
- 834 Kanda M (2006) Large-eddy simulations on the effects of surface geometry of  
835 building arrays on turbulent organized structures. *Boundary-Layer Meteorol*  
836 118(1):151–168
- 837 Kanda M, Moriwaki R, Kasamatsu F (2004) Large-eddy simulation of turbulent  
838 organized structures within and above explicitly resolved cube arrays. *Boundary-*  
839 *Layer Meteorol* 112(2):343–368
- 840 Kanda M, Inagaki A, Miyamoto T, Gryschka M, Raasch S (2013) A new aero-  
841 dynamic parametrization for real urban surfaces. *Boundary-Layer Meteorol*  
842 148(2):357–377
- 843 Macdonald R, Griffiths R, Hall D (1998) An improved method for the estimation  
844 of surface roughness of obstacle arrays. *Atmos Environ* 32(11):1857–1864
- 845 Nakajima C, Mitsuta Y, Tanaka M (1979) Ujigawa meteorological tower for  
846 boundary layer monitoring. *Annals of Disaster Prevention Research Institute*  
847 22B(2):127–141
- 848 Nakayama H, Takemi T, Nagai H (2011) Les analysis of the aerodynamic surface  
849 properties for turbulent flows over building arrays with various geometries. *J*  
850 *Appl Meteorol Clim* 50(8):1692–1712
- 851 Nakayama H, Takemi T, Nagai H (2012) Large-eddy simulation of urban boundary-  
852 layer flows by generating turbulent inflows from mesoscale meteorological sim-  
853 ulations. *Atmos Sci Lett* 13(3):180–186

- 
- 854 Nakayama H, Leitl B, Harms F, Nagai H (2014) Development of local-scale high-  
855 resolution atmospheric dispersion model using large-eddy simulation. part 4:  
856 turbulent flows and plume dispersion in an actual urban area. *J Nucl Sci Technol*  
857 51(5):626–638
- 858 Nakayama H, Takemi T, Nagai H (2015) Large-eddy simulation of turbulent winds  
859 during the Fukushima Daiichi nuclear power plant accident by coupling with a  
860 meso-scale meteorological simulation model. *Adv Sci Res* 12(1):127–133
- 861 Nakayama H, Takemi T, Nagai H (2016) Development of local-scale high-  
862 resolution atmospheric dispersion model using large-eddy simulation. part 5:  
863 detailed simulation of turbulent flows and plume dispersion in an actual urban  
864 area under real meteorological conditions. *J Nucl Sci Technol* 53(6):887–908
- 865 Oikawa S, Meng Y (1995) Turbulence characteristics and organized motion in a  
866 suburban roughness sublayer. *Boundary-Layer Meteorol* 74(3):289–312
- 867 Oke TR (1988) Street design and urban canopy layer climate. *Energy Build*  
868 11(1):103–113
- 869 Park SB, Baik JJ, Han BS (2015) Large-eddy simulation of turbulent flow in a  
870 densely built-up urban area. *Environ Fluid Mech* 15(2):235–250
- 871 Ratti C, Di Sabatino S, Britter R, Brown M, Caton F, Burian S (2002) Analysis  
872 of 3-d urban databases with respect to pollution dispersion for a number of  
873 European and American cities. *Water Air Soil Pollut Focus* 2(5-6):459–469
- 874 Raupach M (1981) Conditional statistics of Reynolds stress in rough-wall and  
875 smooth-wall turbulent boundary layers. *J Fluid Mech* 108:363–382
- 876 Roth M (2000) Review of atmospheric turbulence over cities. *Q J R Meteorol Soc*  
877 126(564):941–990

- 878 Shaw RH, Tavangar J, Ward DP (1983) Structure of the reynolds stress in a canopy  
879 layer. *J Clim Appl Meteorol* 22(11):1922–1931
- 880 Smagorinsky J (1963) General circulation experiments with the primitive equa-  
881 tions: I. the basic experiment. *Mon Weather Rev* 91(3):99–164
- 882 Stoll R, Porté-Agel F (2006) Effect of roughness on surface boundary conditions  
883 for large-eddy simulation. *Boundary-Layer Meteorol* 118(1):169–187
- 884 Wallace JM (2016) Quadrant analysis in turbulence research: history and evolu-  
885 tion. *Annu Rev Fluid Mech* 48:131–158
- 886 Xie ZT (2011) Modelling street-scale flow and dispersion in realistic windsto-  
887 wards coupling with mesoscale meteorological models. *Boundary-Layer Meteorol*  
888 141(1):53–75
- 889 Xie ZT, Castro IP (2009) Large-eddy simulation for flow and dispersion in urban  
890 streets. *Atmos Environ* 43(13):2174–2185
- 891 Xie ZT, Coceal O, Castro IP (2008) Large-eddy simulation of flows over random  
892 urban-like obstacles. *Boundary-Layer Meteorol* 129(1):1–23
- 893 Zaki SA, Hagishima A, Tanimoto J, Ikegaya N (2011) Aerodynamic parameters  
894 of urban building arrays with random geometries. *Boundary-Layer Meteorol*  
895 138(1):99–120
- 896 Zhu X, Iungo GV, Leonardi S, Anderson W (2017) Parametric study of urban-like  
897 topographic statistical moments relevant to a priori modelling of bulk aerody-  
898 namic parameters. *Boundary-Layer Meteorol* 162:231–253



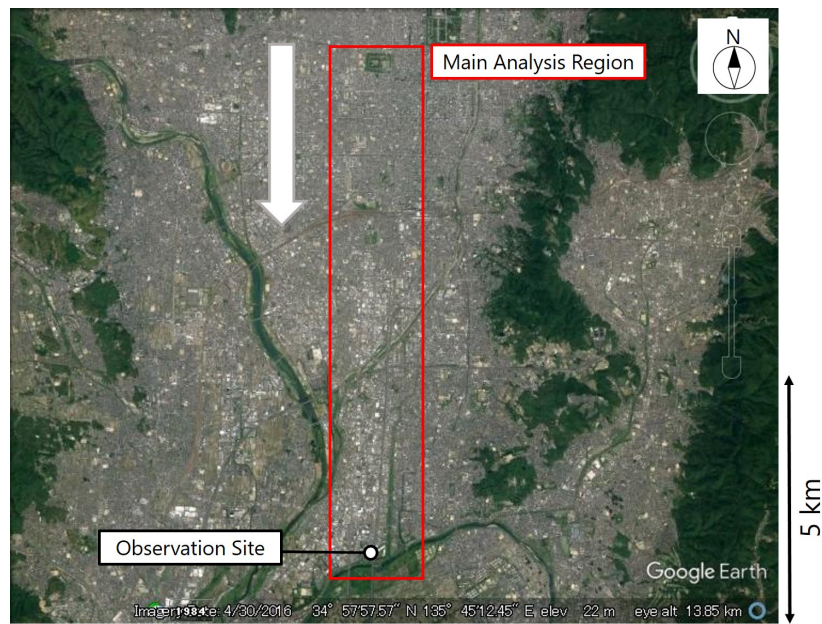


**Fig. 1** The study area in which the LES model and observations were carried out is indicated by the red box. The observational site of the Disaster Prevention Research Institute, Kyoto University, is indicated by the white circle. The white arrow indicates the streamwise wind direction. The satellite picture is taken from Google Earth.

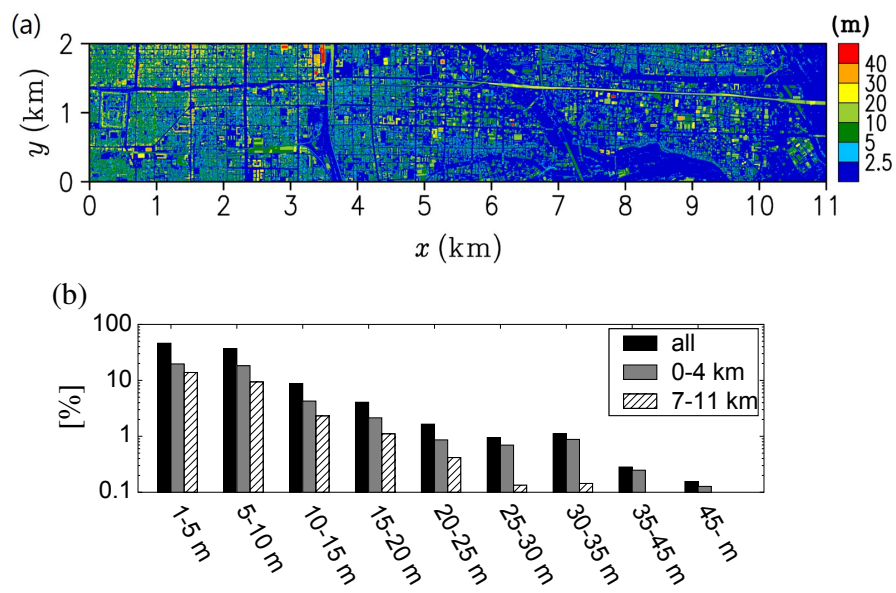


**Fig. 2** (a) Distribution of building and structure heights in the analysis region of Kyoto. (b) Frequency distribution of building heights in the analysis region. The black bar indicates the frequency distribution of buildings in the overall region, while the grey and hatched bars indicate the frequency distributions of buildings in the regions with  $x = 0 - 4$  km and with  $x = 7 - 11$  km, respectively.

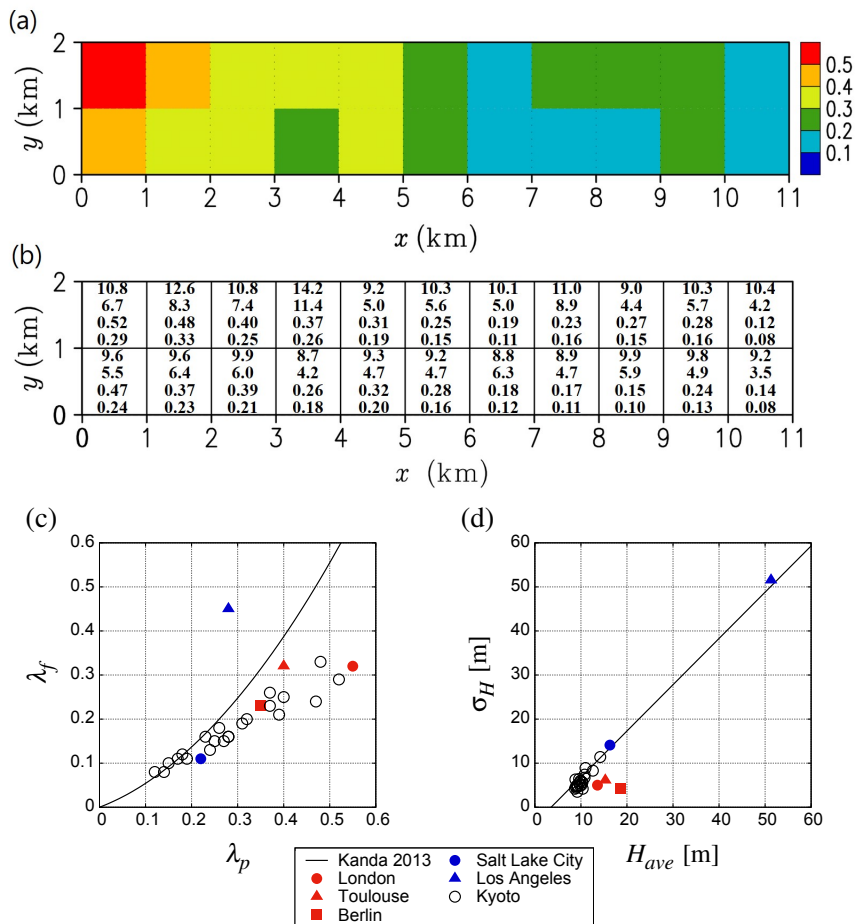


**Fig. 3** (a)  $\lambda_p$  calculated for 1 km by 1 km areas over the analysis region. (b) Roughness parameters calculated for 1 km by 1 km areas over the analysis region. In each box, the first row is  $H_{ave}$ , the second is  $\sigma_H$ , the third is  $\lambda_p$ , and the fourth is  $\lambda_f$ . Scatter plots (c) between  $\lambda_p$  and  $\lambda_f$  and (d) between  $\sigma_H$  and  $H_{ave}$ . The black lines in (c) and (d) indicate the empirical relationships derived from Tokyo and Nagoya, respectively, by Kanda et al. (2013). The values of Salt Lake City and Los Angeles in North America and London, Toulouse, and Berlin in Europe, as indicated by the lower legend, are obtained from Ratti et al. (2002).

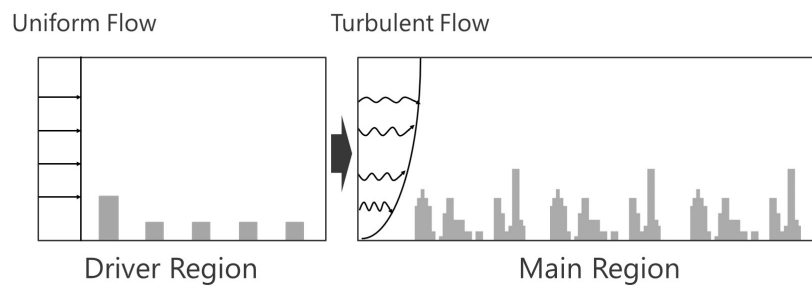


**Fig. 4** Schematic of turbulent flows formed in the driver region and imposed on the main region as the inflow condition.

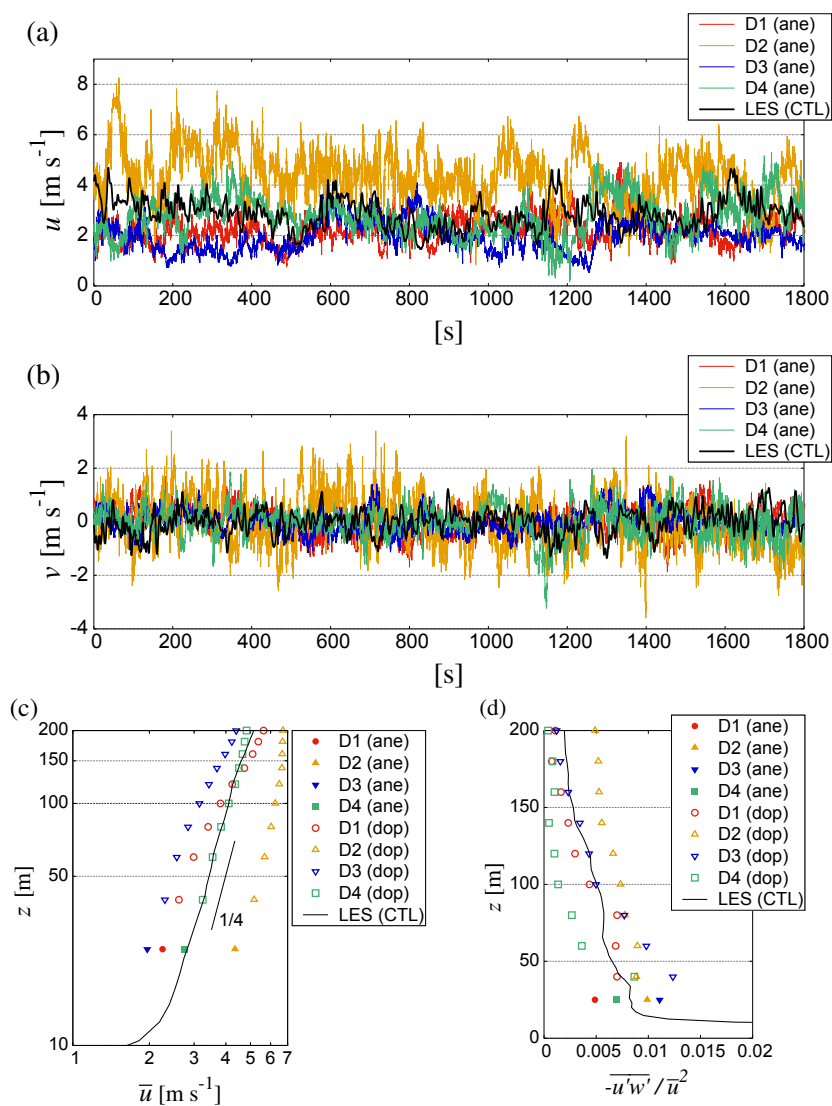


**Fig. 5** Time series of (a) streamwise and (b) spanwise velocity components at 25-m height observed by the sonic anemometer during periods D1 – D4 and simulated by the LES model. Vertical profiles of (c) mean streamwise velocity component and (d) Reynolds stress normalized by the mean streamwise velocity component in the observations and the LES results. Note that the profiles in (c) are plotted on logarithmic axes. A line with a slope 1/4 is also plotted for reference. Here, ‘ane’ and ‘dop’ refer to the observations by the anemometer and Doppler lidar, respectively.

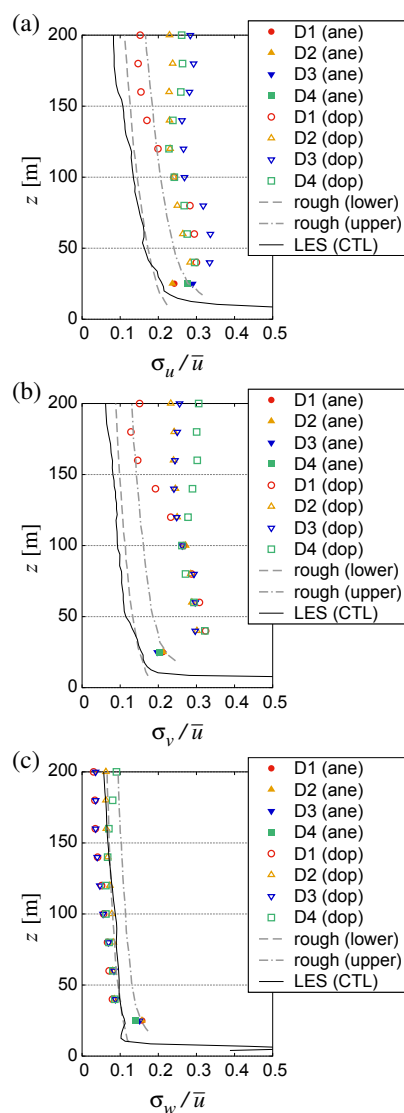


**Fig. 6** Vertical profiles of turbulence intensity from the observations, the LES model, and the empirical profiles provided by the ESDU (1985) for the (a)  $u$ , (b)  $v$ , and (c)  $w$  components. The dashed and dashed-dotted lines indicate the upper and the lower limits, respectively, of the rough-surface class based on the ESDU (1985).

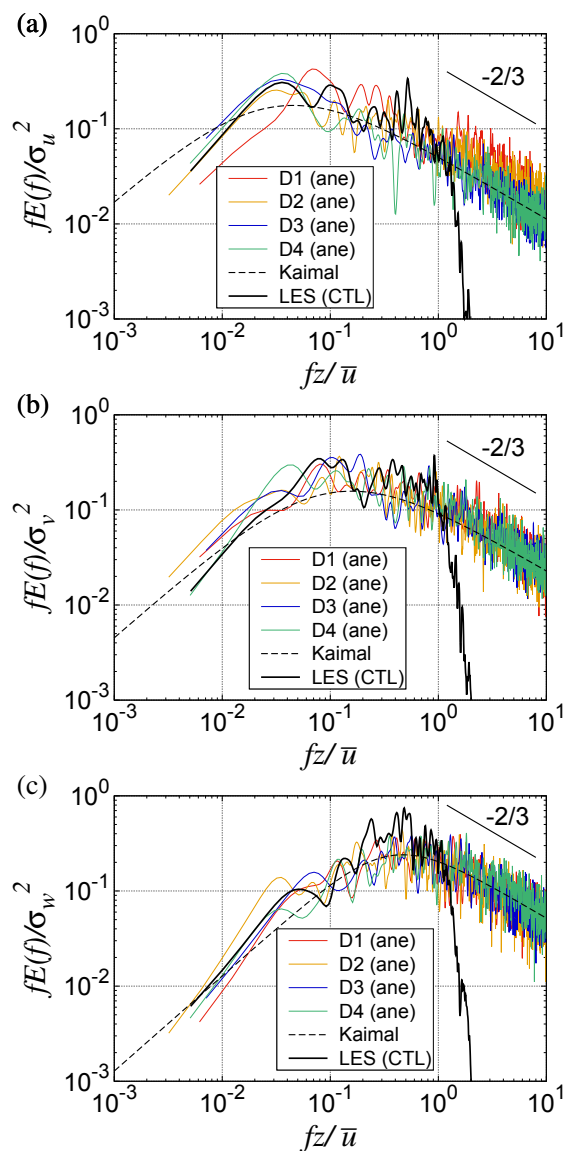


**Fig. 7** Power spectra obtained from the sonic anemometer and the LES model at 25-m height plotted on logarithmic axes: (a)  $u$ , (b)  $v$ , and (c)  $w$  components. The dashed line indicates the empirical profile over a rural surface proposed by Kaimal et al. (1972).

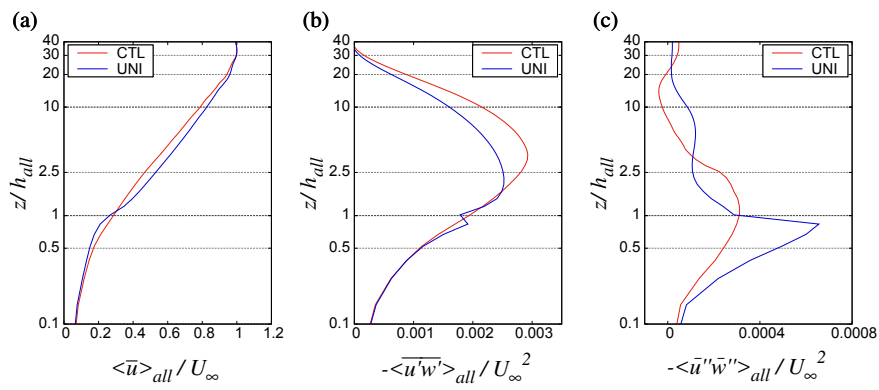


**Fig. 8** Vertical profiles of (a) time-averaged streamwise velocity component, (b) Reynolds stress, and (c) dispersive flux averaged spatially over the main region. These values are normalized by  $U_\infty$ . Red and blue lines denote the result of the CTL and UNI experiments, respectively. The vertical axis is normalized by  $z = h_{all}$ . Note that a logarithmic scale is used for the vertical axis.



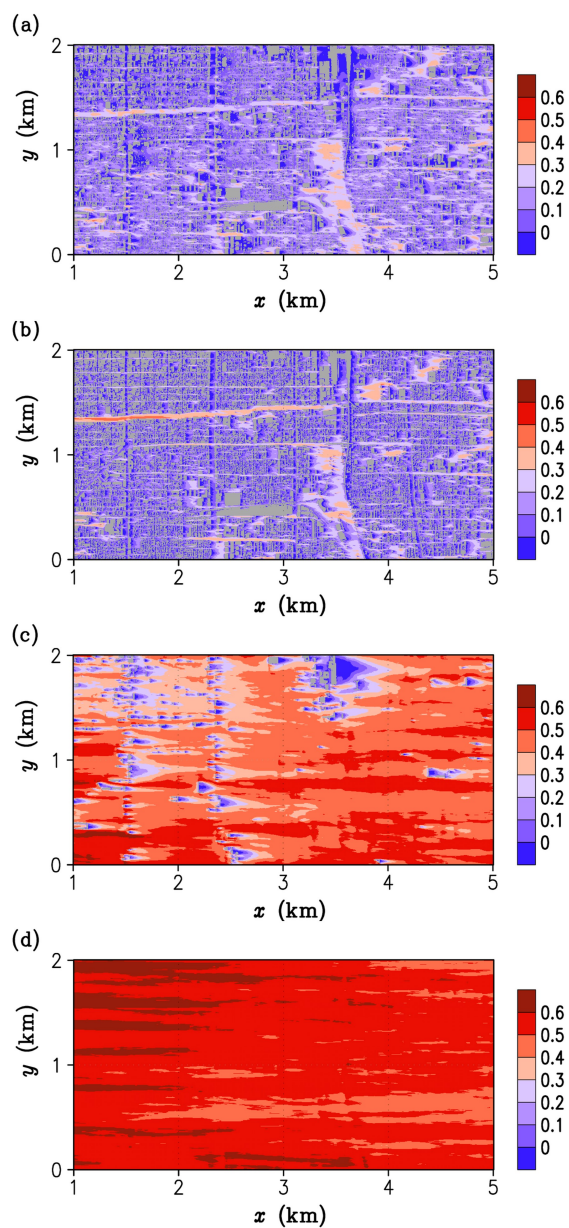


**Fig. 9** Horizontal cross sections of the time-averaged streamwise velocity component normalized by  $U_\infty$  in (a) the CTL experiment at height  $z = 0.5h_{all}$ , (b) the UNI experiment at height  $z = 0.5h_{all}$ , (c) the CTL experiment at height  $z = 2.5h_{all}$ , and (d) the UNI experiment at height  $z = 2.5h_{all}$ . An upstream part of the main region is shown. The legend indicating the wind speed is present to the right of each panel. The grey shading indicates buildings.

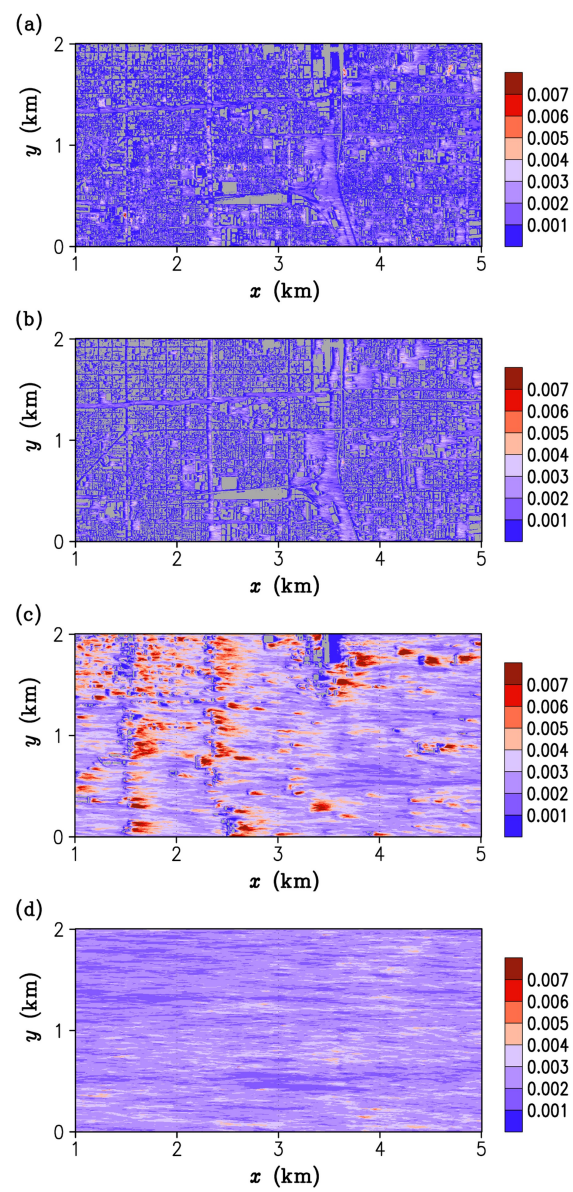
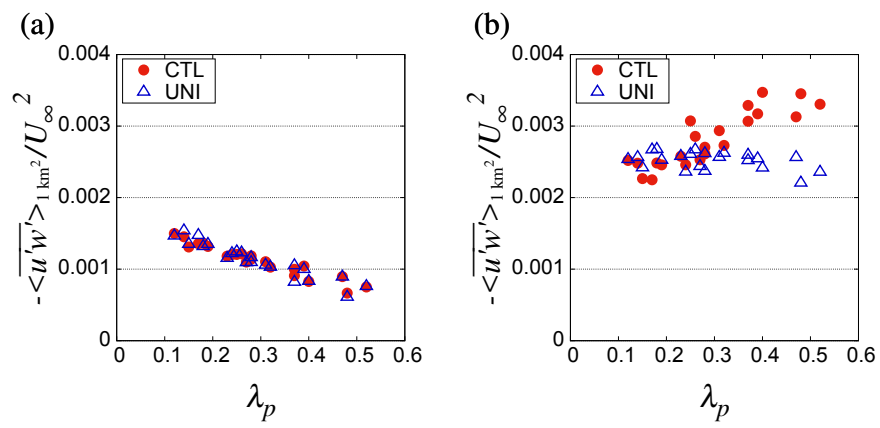
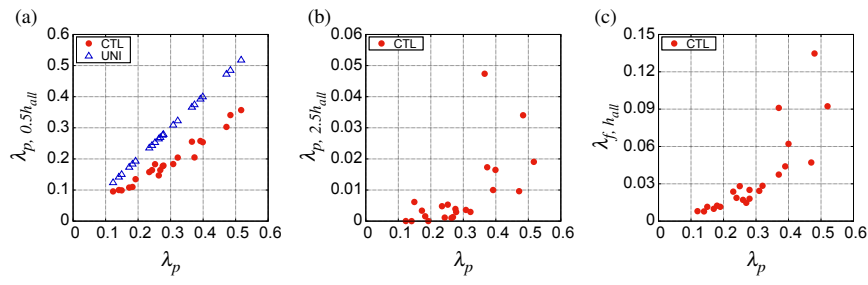


Fig. 10 As Fig. 9, except with the corresponding Reynolds-stress results.



**Fig. 11** Variations of Reynolds stress normalized by  $U_\infty$  with  $\lambda_p$  at heights (a)  $z = 0.5h_{all}$  and (b)  $z = 2.5h_{all}$ .



**Fig. 12** Variations of  $\lambda_p$  calculated (a) at height  $z = 0.5h_{all}$  ( $\lambda_{p, 0.5h_{all}}$ ), (b) at height  $z = 2.5h_{all}$  ( $\lambda_{p, 2.5h_{all}}$ ), and (c)  $\lambda_f$  calculated at height  $z = h_{all}$  ( $\lambda_{f, h_{all}}$ ) with  $\lambda_p$  at the surface. Note that the scale of the vertical axis differs by panel.

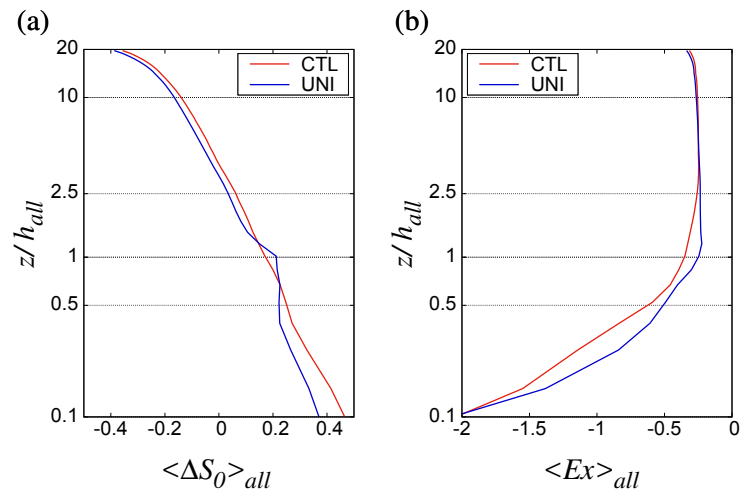


**Fig. 13** Vertical profiles of (a)  $\Delta S_0$  and (b)  $Ex$  averaged spatially over the main region. Red and blue lines denote the results of the CTL and UNI experiments, respectively. The vertical axis is normalized by  $h_{all}$ . Note that a logarithmic scale is used for the vertical axis.

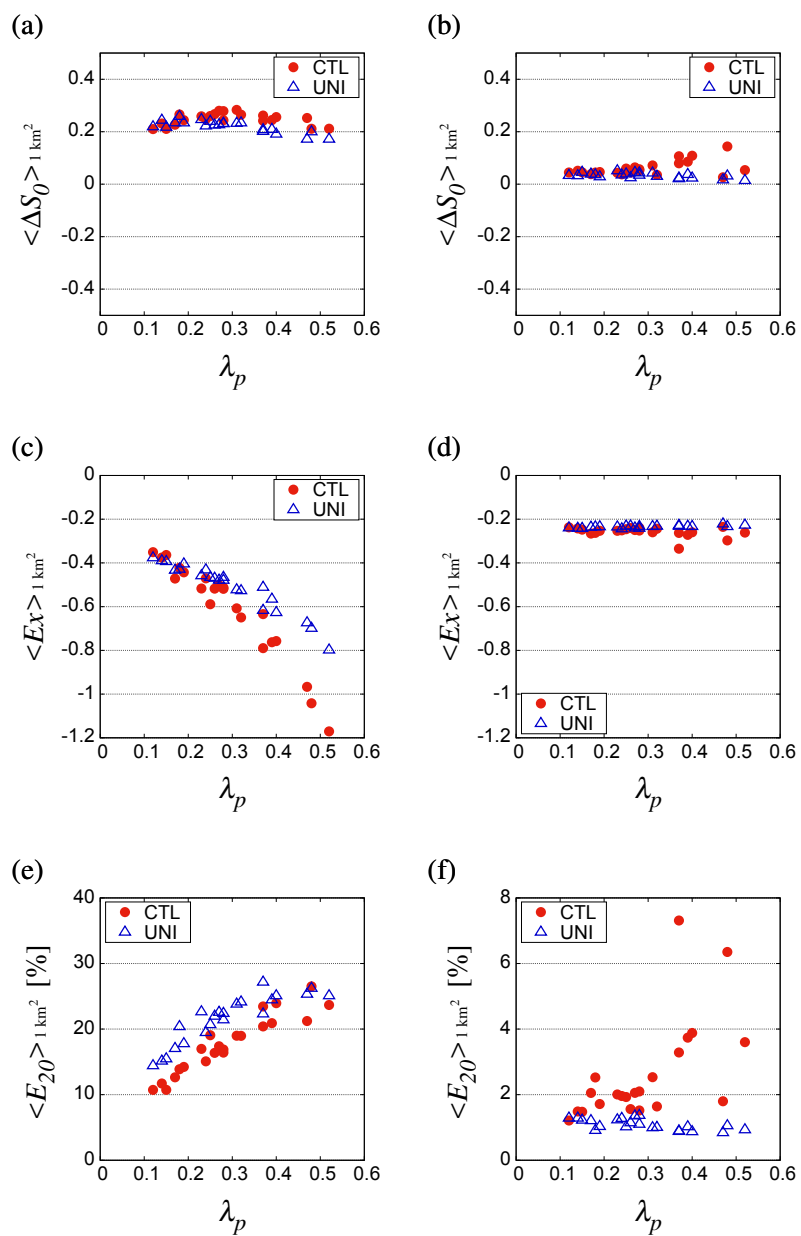


**Fig. 14** Variations of  $\Delta S_0$  with  $\lambda_p$  at (a) heights  $z = 0.5h_{all}$  and (b)  $z = 2.5h_{all}$ ,  $Ex$  at (c) heights  $z = 0.5h_{all}$  and (d)  $z = 2.5h_{all}$ , and  $E_{20}$  at (e) heights  $z = 0.5h_{all}$  and (f)  $z = 2.5h_{all}$ .

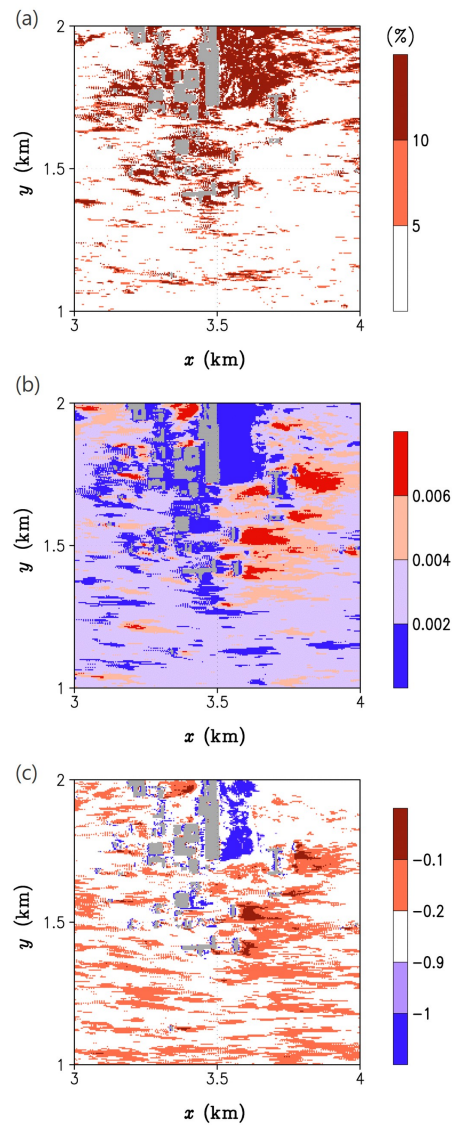


**Fig. 15** Horizontal cross section of (a)  $E_{20}$ , (b) Reynolds stress normalized by  $U_\infty$ , and (c)  $Ex$  at height  $z = 2.5h_{all}$  over a 1 km by 1 km area within the business district in the CTL experiment. The grey shading indicates buildings.